N84-23691

NASA Technical Memorandum 83598

Ground Correlation Investigation of Thruster Spacecraft Interactions to be Measured on the IAPS Flight Test

John L. Power
Lewis Research Center
Cleveland, Ohio .

NASA

GROUND CORRELATION INVESTIGATION OF THRUSTER/SPACECRAFT INTERACTIONS
TO BE MEASURED ON THE IAPS FLIGHT TEST

John L. Power*
National Aeronautics and Space Administration
Lewis Research Center
Cleveland, Ohio, U. S. A.

E-2007

Abstract

Preliminary ground correlation testing has been conducted with an 8-cm mercury ion thruster and diagnostic instrumentation replicating to a large extent the IAPS flight test hardware, configuration, and electrical grounding/ isolation. Thruster efflux deposition retained at 25° C was measured and characterized. Thruster ion efflux was characterized with retarding potential analyzers. Thruster-generated plasma currents, the spacecraft common (SCC) potential, and ambient plasma properties were evaluated with a spacecraft potential probe (SPP). All the measured thruster/ spacecraft interactions or their IAPS measurements depend critically on the SCC potential, which can be controlled by a neutralizer ground switch and by the SPP operation.

Abbreviations and Symbols

See Table II for thruster performance parameter symbols.

BF	Full beam (thruster mode)
CC	Cathode conditioning (thruster mode)
DSH	Deposition slide holder
e	Electronic charge (1.592×10^{-19} C)
e⁻	Electron (current)
EM	Engineering model
Hg	Mercury
Hg^+	Mercury ion (singly charged)
Hg^{+2}	Mercury ion (doubly charged)
i^+	Ion (current)
I_{IB}	ICD biasing grid current
I_{IC}	ICD collector plate current
I_{IS}	ICD shielding-suppressor grid current
I_{IT}	Total ICD current (= Σ I_{IB}, I_{IC}, and I_{IS})
I_{PP}	SPP current
IAPS	Ion Auxiliary Propulsion System
ICD	Ion collector detector
k	Boltzmann's constant (1.381×10^{-16} erg K^{-1})
m_e	Electron mass (9.11×10^{-28} g)
m_i	Ion mass
Mo	Molybdenum
Mo^+	Molybdenum ion (singly charged)
MoS_2	Molybdenum disulfide (lubricant)
ϕ	Floating potential
PPU	Power processor unit
QCM	Quartz crystal microbalance
SCC	Spacecraft common
SCM	Solar cell monitor
SMSS	Spacecraft module surface simulator
SPP	Spacecraft potential probe
SS	Steady state standby (thruster mode)
T_e	Electron temperature (Maxwellian)
T_i	Ion temperature (Maxwellian)
TGBSU	Thruster-gimbal-beam shield unit
v_i	Ion drift velocity

---

*Aerospace Engineer.

V_{IB-G}	ICD biasing grid potential, referred to tank-ground
V_{IB-P}	ICD biasing grid potential, referred to ambient plasma potential
V_{IB-S}	ICD biasing grid potential, referred to SCC
V_{IS-G}	ICD shielding-suppressor grid potential, referred to tank ground
V_{IS-P}	ICD shielding-suppressor grid potential, referred to ambient plasma potential
V_{IS-S}	ICD shielding-suppressor grid potential, referred to SCC
V_{P-G}	Ambient plasma potential, referred to tank ground
V_{PP-G}	SPP potential, referred to tank ground
V_{PP-S}	SPP potential, referred to SCC
V_{S-G}	SCC potential, referred to tank ground
V_{S-P}	SCC potential, referred to ambient plasma potential
+X	Spacecraft axis aligned with velocity vector, opposite to IAPS module
-X	Spacecraft axis aligned with velocity vector, towards IAPS module
-Z	Spacecraft axis aligned with earth line, zenith direction

Introduction

The Ion Auxiliary Propulsion System (IAPS) flight test will flight qualify an 8-cm diam., 5 mN mercury ion thruster subsystem for auxiliary propulsion applications on future spacecraft. In particular, the subsystem is designed for north-south stationkeeping of geostationary communications satellites. Specific goals of the flight test are: (1) to demonstrate reliable thruster operation over a typical mission profile requiring 7055 hr thrusting in 2557 cycles, (2) to make in-flight measurements of thruster/spacecraft interactions pertaining to flight applications; and (3) to demonstrate compatibility during simultaneous operation of two thrusters. The flight hardware and its configuration are discussed in the following section. All aspects of the flight test are described in detail in Refs. 1-3.

Electron bombardment thruster/spacecraft interactions have been classified and the literature available on them has been reviewed by Byers.[4] The interactions measured in the IAPS flight test comprise contamination and plasma effects. Kaufman and Carruth[5] have modeled these interactions in terms of the effects of the thruster-generated charge exchange plasma on spacecraft solar cell arrays. Deposition of non-volatile efflux during extended ground operation of a 5-cm diam. mercury ion thruster has been characterized by Weigand and Mirtich.[6]

In support of the IAPS flight test, a ground correlation test program is being conducted to evaluate the thruster/spacecraft interactions measured in the flight test and to characterize the flight detectors. The thruster, diagnostic

instruments, experimental configuration, and environmental conditions in the ground testing closely replicate those of the flight test, as discussed subsequently. The ground measurements are therefore expected to correlate accurately with the flight test results. Subsequent phases of the ground testing will seek to three-dimensionally measure and model the investigated interactions and determine the effects on them due to varying the environmental conditions, the thruster operation, etc. This paper presents and analyzes preliminary results obtained in the initial phase of the ground test program.

The following sections of the paper describe: the flight and ground test experimental apparatus, including the design and operation of the detectors employed; the thruster and facility operation; and the interaction measurements obtained, with consideration of their self-consistency and the adequacy of the flight detector designs for the required flight measurements. A final section summarizes the principal results and conclusions from the testing performed.

Abbreviations and symbols used throughout the paper are compiled in the foregoing section, except that symbols for thruster operating and performance parameters are given in Table II. As noted in the abbreviations and symbols listing, voltages involved in the diagnostics measurements and operation are identified by two hyphenated subscripts, the first denoting the generic potential and the second giving the reference ground for the potential measurement.

Flight Test Apparatus, Configuration, and Measured Interactions

The spacecraft configuration of the IAPS flight hardware is shown in Fig. 1. The flight package consists of two thruster subsystems, mounted on the $-X$ and $-Z$ spacecraft surfaces, and a diagnostics subsystem comprising detectors arrayed about both thrusters. The spacecraft is depicted as deployed and 3-axis stabilized in its final 740-km circular, high-inclination orbit. The spacecraft velocity vector shown applies during one-half of the on-orbit operation. This vector is reversed, by yawing the spacecraft, to be in exactly the opposite direction the remainder of the time.

The thruster/spacecraft interactions actively measured during the flight test and in the ground testing are listed in Table I. The interactions are classified either as depositional or as electrical in nature. The table gives the type and number of detectors measuring each interaction, the measurement effect or analytical process by which the interaction magnitude is determined from the detector data, and the estimated lower detection limit of each detector. This information is given for both the flight detectors and the detectors employed in the ground correlation testing.

The depositional interactions identified in Table I comprise thruster efflux retained at ambient temperatures (25° C) and at cold temperatures ($\lesssim -60°$ C). The species retained at ambient temperature are nonvolatile materials such as molybdenum sputtered from the thruster accelerator grid. The species retained at cold temperatures may in addition include volatile materials, such as mercury propellant from the thruster.

The flight instruments employed to measure deposition retained at 25° C include temperature-controlled quartz crystal microbalances (QCM's) and solar cell monitors (SCM's) which are heat sunk to the spacecraft. SCM's which are thermally isolated from the spacecraft and cooled by attached radiators are used in the flight test to measure deposition retained at cold temperatures. In addition, this interaction is also measured by any degradation observed in the radiator cooling performance arising from deposition retained on the radiator surfaces. As indicated in the table, the sensitivities of the flight instruments measuring deposition vary widely, from the very high sensitivity of the QCM's to the much lower sensitivity of the SCM's, with the radiator sensitivity intermediate.

The electrical interactions identified in Table I are measured by an array of ion collector detectors (ICD's) and by a single spacecraft potential probe (SPP). Thruster-generated ion fluxes to spacecraft surfaces are characterized with the ICD's, which are wide-angle, Faraday-cup, retarding potential analyzers providing ion energy discrimination at four retarding potential levels. The electron currents to biased surfaces are evaluated as a function of the biasing potential by the large-area, spherical SPP. Langmuir curve analysis of the SPP current-voltage data also gives the spacecraft potential, which is determined relative to the ambient space plasma potential. The spacecraft potential is a true thruster/spacecraft interaction since it is controlled not by environmental conditions but by the thruster operation and electrical configuration. Specifically, the spacecraft potential is determined by the coupling of the thruster ion and electron efflux to the spacecraft surfaces and to the ambient space plasma, with a neutralizer grounding switch providing the option of short circuiting the plasma coupling to the spacecraft.

A photograph showing the configuration of the flight diagnostic devices about the zenith ($-Z$ spacecraft surface) thruster is presented in Fig. 2. Except for the inboard ICD and the SPP, all of the detectors are located at a basic radial distance of 60 cm from the thruster axis. At this distance, the 8 cm thruster acts effectively as a point or axial source of the measured effluent species. Thus, these detectors make far-field measurements of the interactions. The ICD array also provides comparable measurements assessing the ion flux and energy variation with radial distance and divergence angle from the thruster axis.

Each flight thruster subsystem consists of the components shown in Fig. 3. Power and propellant are furnished to the thruster by the power electronics unit and the propellant tank, respectively. The digital controller and interface unit provides the power, command, and telemetry interface of the subsystem with the spacecraft. It also contains software for autonomous and manual thruster/gimbal operations initiated via commands from the spacecraft. The thruster with its attached beam shield is seen mounted on a gimbal in an integrated thruster-gimbal-beam shield unit (TGBSU). The neutralizer is situated on the beam shield midplane in the maximally shielded location.

The beam shield on each IAPS thruster is not required for purposes of the flight test. It will, however, likely be required in subsequent flight applications of the thruster subsystem, such as in spacecraft body-mounted configurations for north-south stationkeeping, to shield sensitive spacecraft surfaces or solar arrays from thruster efflux, both neutral and charged. Because of this likelihood, a beam shield is incorporated on each flight test thruster. Each shield has a conductive molybdenum coating and is electrically isolated from all other structures.

The detector configuration about each flight thruster is substantially affected by the assymmetric shielding effects of the thruster beam shield. As seen in the Fig. 2 zenith spacecraft module configuration, a QCM and a warm SCM are mounted on the high boom in back of the beam shield. These detectors measure ambient-temperature deposition at locations within, but near the edge of the beam shield umbra cast for line-of-sight efflux from the thruster accelerator grid. The detectors thus evaluate deposition on spacecraft surfaces or solar arrays which are similarly situated in thruster application configurations. Also as may be seen in Fig. 2., the ICD and SCM arrays in the flight test are arranged to provide comparable data directly evaluating the effectiveness of the beam shield in reducing the magnitudes of the electrical and depositional interactions. The SPP location was chosen so that the required separation of the probe sphere from all spacecraft potential surfaces could be achieved with the sphere fully shielded by the beam shield from line-of-sight thruster efflux.

Ground Test Apparatus, Configuration, and Detector Descriptions

Test Apparatus and Facility

The ground correlation testing was performed with the experimental apparatus shown in Fig. 4. Two new detectors, known as deposition slide holders (DSH's), may be seen. These detectors, as subsequently described, have been used in the ground testing in place of the warm SCM's of the flight diagnostics subsystem. The TGBSU employed in the ground testing is an 8-cm engineering model (EM) assembly retrofitted to closely duplicate the IAPS flight TGBSU's. It is mounted by its gimbal from a spacecraft module surface simulator (SMSS) which closely duplicates the flight test -Z module in physical dimensions, configuration, surface treatment, and the size and location of wire mesh ground planes extending out from the TGBSU under all the detectors.

The TGBSU is mounted and aimed so that the thruster axis is congruent with the axis of the vacuum tank employed for the testing. This tank, located at the NASA Lewis Research Center, is 3.0 m in diameter by 5.9 m long and is horizontally oriented. The thruster ion beam is directed into a 1.0 m diam. graphite target located at the opposite end of the vacuum tank. The target is grounded to the tank structure.

The vacuum tank is pumped by six 81 cm diffusion pumps, each equipped with a liquid nitrogen-cooled baffle to minimize backflow into the tank of residual amounts of the silicone pump oil. The tank is also cryopumped by a baffle at the end of the tank behind the graphite beam target. This baffle was partially cooled by a restricted flow of liquid nitrogen. Cylindrical cryoliners along the inside circumference of the tank were not cooled in the testing.

Plan and elevation drawings specifying the locations of the diagnostic instruments relative to the thruster and beam shield are presented in Figs. 5(a), (b), and (c) for the ground test apparatus. These locations and the detector orientations duplicate those of the corresponding instruments in the IAPS flight package.[2] Each of the detectors, except for the SPP, has an axis of symmetry which gives its aiming direction. The intersection of this axis with the front surface, grid, or aperture of the detector defines the detector location indicated in Figs. 5(a), (b), and (c). All of the detectors, both in the flight and ground test configurations, are aimed at a point on the thruster axis 9 cm downstream of the accelerator grid plane. As in the flight test, the detectors mounted on the high boom are totally within, but near the edge of the beam shield umbra.

Table I details the types and number of detectors used in the ground testing. Each type of ground detector is described below and its differences from the corresponding flight instrument noted.

Deposition Slide Holders

It will be observed in Table I that no instruments have been employed in the ground tests to date to measure thruster efflux deposition retained at cold temperatures. This interaction will be measured in the flight test by the cold SCM's and their radiators. Evaluation of this interaction using exposed SCM's and radiators, at either warm (25° C) or cold temperatures, is subject to large errors in ground correlation tests due to facility effects.

Because of the facility effect problem, the SCM measurements at ambient (25° C) temperatures were performed instead with two DSH's. These instruments, which are shown in Fig. 6, are evacuated boxes each holding a glass slide with approximately 50 percent of its area masked by a tantalum mask. Each detector has a shutter which is vacuum-tight in its closed position. This may be remotely actuated under vacuum via a double-acting pneumatic cylinder so that in its open position the slide and mask are exposed through a small-area aperture in the shutter diaphragm. The advantage of the DSH design is that the shutter may be kept closed and the slide and mask protected during vacuum tank operations, such as pumpdown and bleed-up, which can cause substantial contaminant deposition.

Before being mounted for testing, the assembled DSH's were evacuated through the side valve seen in Fig. 6, using a well-trapped diffusion pump. During the testing, the shutter of each detector was opened only with the thruster in steady-state full beam (BF) operation and was closed before the BF operation was terminated. Each detector was maintained at 25° C during the testing by means of an attached thermocouple and heater. The integrated total deposition retained

on each slide and mask was determined afterwards from their weight gains. Though the DSH design, operation, and orientation were intended to minimize spurious, facility-caused deposition effects, measurements have not yet been obtained verifying that the weight gains determined for the DSH masks and slides are actually attributable to just the direct deposition of thruster-generated efflux. A preliminary test of the DSH's without any thruster operation indicated no measurable deposition was retained at 25° C on the DSH slides and masks due to vacuum tank operation at high vacuum conditions.

Quartz Crystal Microbalance

The QCM mounted on the high boom was also employed for measuring deposition retained at ambient temperatures. The ground correlation detector differs from the IAPS flight instruments in having detector and reference crystals which oscillate at 15 MHz, instead of the 10 MHz frequency of the the flight QCM's. The higher oscillation frequency gives the ground detector a higher beat frequency response to retained deposition. For the ground QCM this response is 0.64 Hz $(ng \ cm^{-2})^{-1}$, compared to a response of 0.23 Hz $(ng \ cm^{-2})^{-1}$ for the flight QCM's. As in the flight test, the ground QCM was always operated with its detector and reference crystals maintained at 25.0 (+ 0.1)° C by means of a Peltier thermoelectric element and control circuit. The ground QCM has the capability for temperature-controlled operation up to 100° C. This capability was utilized for extended periods during the testing to bake off volatile contaminants on the crystals under vacuum. As with the DSH's, it was found that normal vacuum tank operation at high vacuum, without the thruster running, caused no detectable deposition on the QCM at 25° C.

The QCM beat frequency was counted over successive 10 sec intervals, and the least significant 100 Hz of the frequency was continuously plotted on a strip chart recorder. This allowed determination of very low deposition rates from constant, small frequency slopes observed over periods of many hours during steady state thruster operation.

Ion Collector Detectors

The three ICD's utilized for the ground measurements of thruster-generated ion fluxes are identical to the flight detectors[3] in physical design, preamplifier and autoranging circuitry, and overall range. They are wide-angle, large-area, retarding potential ion collectors. Details of the detector design are shown in Fig. 7.

The four grids of each ICD, equally spaced in front of the collector plate, have the following functions. The outermost or grounding grid establishes a ground plane at the detector case (and collector plate) potential to minimize detector perturbation of the adjacent external plasma. The second or shielding grid is negatively biased from the case potential to reflect incoming electrons. In the flight ICD's, the shielding grid voltage is fixed at −12 V from the case potential; in the ground testing this voltage was varied from 0 to −21 V. The third or biasing grid is positively biased from the case potential to reflect incoming positive ions having kinetic energy insufficient

to overcome the electrostatic repulsive force created. In the flight ICD's, biasing grid voltages of 0, +25, +55, and +96 V (from the case potential) may be selected; in the ground testing the voltage was set at any desired value over the same range. The selected biasing grid voltage is common to all the ICD's, both in the ground and the flight detector operation. The innermost or suppressor grid is electrically common with the shielding grid in the detector. It serves the function of repelling back to the collector plate any secondary or photo-electrons produced at the collector plate. This prevents escaping electrons from erroneously adding to the collected ion current read.

The four grids of each ICD are accurately machined and indexed relative to each other to minimize physical interception of incoming ions. The open area fraction of each grid is ~72%. The 1.6 mm mesh opening dimension of the grids is calculated to be significantly less than the DeBye shielding length existing under any plasma conditions in which the detectors will be used. This insures maximum planarity of the equipotential surfaces between the grids.

The ICD's measure collector plate currents on six linear decade ranges with full-scale values of 1×10^{-3} to 1×10^{-8} A. The detector electronics auto-ranges to the proper range to read 8–100 percent of the full scale value. In practice, the lowest range provides reliable readings down to ~1 percent of full scale (i.e., ~1×10^{-10} A). In the ground testing, the collected current signals for each ICD were continuously recorded on a strip chart. This allowed characterization of transient responses of the detectors to altered plasma conditions, e. g., from changes in thruster operation. The diagnostic circuitry for the ground testing includes a digital electrometer by which the positive or negative current collected on the shielding-suppressor grids or on the biasing grid of any of the ICD's may be read. In the flight test only the ICD collector plate currents are measured.

The shielding-suppressor grids of all the ICD's in the ground testing are biased in parallel by a single voltage-regulating power supply, as is true of the detectors in the flight test. The biasing grids of all the ground detectors are similarly biased in parallel by a second voltage-regulating power supply, also as in the flight case. A second digital electrometer in the ground test electronics enables accurate measurements to be made of both the ICD shielding-suppressor and biasing grid voltages.

As indicated in Fig. 7, each ICD has a preamplifier to amplify the collector plate current signal. This is located within the detector housing and has the shortest possible input lead from the collector plate, in order to minimize noise pickup and other signal distortions. To eliminate temperature as a possible variable affecting the preamplifier performance and calibration, each ICD in the ground testing was maintained at 25° C during operation by means of a thermocouple and heater mounted on its case.

The 3 ICD locations in the ground testing afford direct measurement comparisons quantifying

(1) the effectiveness of the thruster beam shield in reducing thruster-generated ion fluxes upstream of the grid plane and (2) the ion flux variation with divergence angle from the thruster axis at divergence angles around 90°. All three ICD's in the ground testing were located at the basic detector radial distance of 60 cm from the thruster axis.

Spacecraft Potential Probe

The SPP was employed in the ground testing to measure the electron currents collected on biased surfaces. The probe data was also used to determine the potential, electron temperature, and density of the ambient plasma. The ground detector is identical to the IAPS flight detector[3] in size (24.2 cm diam., 1833 cm^2 area), gold coating, mounting from the SMSS (with a minimum separation of 25 cm from the sphere to the SMSS ground plane), and location relative to the thruster (fully shielded from the grids by the beam shield). For the ground testing, a thermocouple and equatorial heater mounted on the probe were employed to maintain it at 25° C at all times. This was done to prevent mercury condensation on the probe sphere.

The SPP is designed to function as a spherical Langmuir probe with a thin plasma sheath. During the testing performed it was operated as a net electron current collector by being biased positively and negatively from SCC. The probe biasing was provided either by a current-controlling supply like that employed with the flight probe or by an alternate voltage-controlling supply covering the same current range. The ground and flight current-controlling supplies each have 16 selectable current levels spaced at equal logarithmic intervals over the range from 1 μA to 5 mA. In the ground testing using either power supply, the probe potential was maintained between -40 and +205 V, relative to SCC. This is also the available bias range for the flight probe. The SPP bias voltage and net collected current were measured (nonsimultaneously) during the ground testing with the digital electrometers in the diagnostics circuitry.

Electrical Schematic and Configurations

Figure 8 shows an electrical schematic for the tested thruster-power processor-diagnostics circuitry. The diagram emphasizes the grounding and isolation of the various components and indicates the principal ion (i^+) and electron (e^-) plasma currents discussed subsequently with the test results. As seen in the figure, the ground test electrical circuit provides an independent common ground, called spacecraft common (SCC). This is the reference ground for all the diagnostic devices and circuits, except the floating DSH's, and also for the thruster and its power processor. With the grounding switch open, SCC was isolated by $> 10^9$ Ω from the vacuum tank ground. This isolation is important in order to simulate spacecraft electrical conditions in the ground testing, since in the flight test no conduction is possible from the ambient space plasma to SCC (neglecting photoelectric effects) except via plasma ion and electron fluxes reaching SCC surfaces. In the ground testing, the ambient plasma is closely coupled to the tank ground

because of the grounded beam target. Hence with the grounding switch open, the ground test conditions closely simulate the electrical and plasma conditions anticipated in the flight test during thruster operation.

The neutralizer switch seen in Fig. 8 permits thruster operation with the neutralizer either shorted to or isolated from SCC. Each of the flight thruster subsystems has such a switch, enabling the same alternative operation in the flight test. Three electrical configurations may be distinguished for the ground testing, based on the open or closed condition of the grounding and neutralizer switches. These configurations, denoted A, B, and C, are identified on Fig. 8. The preliminary test results reported in this paper are confined to configurations A and B.

In configuration A, with both switches open, SCC floats at a potential determined primarily by the energies of the electrons and ions reaching the surfaces and structures electrically common to SCC. Configuration A simulates the flight test electrical conditions with the neutralizer switch open.

In configuration B, with the grounding switch closed, SCC is shorted to the tank ground and hence is very close to the ambient plasma potential. This configuration, in which thruster ground test operation is ordinarily conducted, is unrepresentative of any flight test operation. Ground test data acquired in this configuration, however, are useful for comparing with and explaining the data taken in the flight-representative configurations.

In configuration C, with the neutralizer switch closed and the grounding switch open, SCC is electrically tied to the neutralizer tip or emitting potential. This neutralizer potential is controlled by the plasma bridge coupling of the neutralizer electron emission to the thruster ion beam. Configuration C simulates the electrical conditions during flight test operation with the neutralizer switch closed.

Effects of Electrical Configurations and SCC Potential

The three electrical configurations and the different SCC potentials in each of them have substantial effects on the measurements and operation of the diagnostic devices. This is equally true of the ground testing and the flight test. In both cases all of the detectors either operate at or are biased from the SCC potential, except for the electrically isolated DSH's in the ground testing and the SCM's in the flight test. The effects of the SCC potential on each of the ground detectors are considered below.

The floating operation of the DSH's simulates the deposition surface conditions of the SCM's and their radiators in the flight test. Ionic species impinging on either type of detector approach at the ambient plasma potential and are either accelerated or decelerated by the potential difference between the plasma and the detector. In the case of the DSH's, this potential difference may focus or defocus the ion flux incident on the shutter aperture, thus increasing or decreasing

the transmitted flux, and it can also substantially affect the adhesion and/or sputtering of the ions as they impinge on the deposition slide and mask.

In both the ground and flight QCM's, the detector crystal surface is electrically common with SCC. The SCC potential, V_{S-p}, referenced from the ambient plasma potential, thus controls the electrostatic acceleration/deceleration of ionic species incident on each QCM and thereby can grossly alter their sticking or sputtering on the detector crystal surface.

In the electrical operation of the ICD's, the SCC potential has important direct effects. These arise from the fact that the ions and electrons entering each detector are at the ambient plasma potential, whereas the shielding-suppressor and biasing grid potentials, V_{IS-S} and V_{IB-S}, are referenced to SCC (as seen in Fig. 8). Therefore, the ions and electrons encounter effective shielding-suppressor and biasing grid potentials, V_{IS-p} and V_{IB-p}, which as referenced to the plasma potential are equivalently altered by the SCC potential, V_{S-p}. V_{S-p} is usually negative (due to a higher electron than ion mobility in the plasma). In such a case V_{IS-p} is increased in magnitude from V_{IS-S}, thereby increasing the capability of the shielding-suppressor grids to reflect electrons. At the same time, V_{IB-p} is equivalently decreased from V_{IB-S}, correspondingly reducing the cutoff energy of the ions which the biasing grid will reflect. If V_{IB-S} does not exceed V_{S-p} in magnitude, V_{IB-p} will be < 0 and the biasing grid will not reflect any incoming ions. The detector collector plate is maintained at the SCC potential. Since this is also the minimum biasing grid potential, the collector plate will collect all ions transmitted by the biasing grid, neglecting interception by the suppressor grid.

The SPP operation and measurements inherently depend on the SCC potential, because in the case of both the flight and ground detectors the probe bias supply is always referenced to SCC. Also, the spacecraft potential determinations made from the probe data are really of the potential difference between SCC and the ambient plasma. Another important effect of SCC on the SPP operation may be seen by tracing the probe electrical circuit in the three configurations indicated on Fig. 8. In all the configurations during ground testing, the full net electron current collected by the SPP must be emitted from the neutralizer. The electrons arrive at the probe either directly from the neutralized ion beam or after thermalization in the vacuum tank. (Any net electron current generated by secondary emission from the beam target and tank walls, due to impingement by energetic beam ions, is balanced by an equivalent electron current from the neutralizer to the tank walls and ground.) Since the SPP is referenced to SCC, the probe circuit must be completed by an equivalent return current from SCC to neutralizer common, which is the neutralizer emitting potential.

During ground testing in configuration A, the SPP return current must be completely supplied by thruster-generated positive ions collected on all the surfaces at the SCC potential. These ions must emanate from the ion beam - essentially all

of them as charge exchange ions produced downstream of the thruster grids. In configuration B, the return current may be partially provided by ion collection on SCC surfaces. But since SCC is grounded to the tank in this configuration, the return current will be predominantly supplied by beam ions impinging on the tank target and walls. Even the highest SPP current level of 5 mA requires only 7 percent of the nominal full thruster beam current of 72 mA to provide the entire return current. In configuration C, a direct short circuit return path exists for the SPP electron current from SCC to neutralizer common, via the closed neutralizer switch. As a result, no ion collection is necessary to complete the probe circuit in this configuration.

When the SPP is operated in either configuration B or C, it acts as a simple Langmuir probe. The data obtained characterize only the electron collection on the probe itself. In configuration A, on the other hand, the SPP and the SCC surfaces act as dual probes. The detector data characterize both the electron collection on the SPP sphere and the balancing ion collection on the surfaces at SCC potential. Separate evaluation of both the electron and the ion collection processes is possible in the ground testing because the SCC potential can be independently measured (from tank ground) and the plasma potential is tied to and essentially constant at a value near the tank ground potential. Such data were taken to characterize both collection processes during SPP operation in configuration A, with the thruster at full beam.

The high (> 10^9 Ω) mutual isolation in the ground test apparatus between the detector circuits, SCC, and tank ground permitted accurate and reproducible floating potentials to be determined. With the instrumentation and leads provided in the ground test experimental setup, the floating potentials of SCC, the beam shield interior surface, and the SPP sphere could be measured. The values obtained during full beam thruster operation are subsequently presented and analyzed.

Results and Discussion

Thruster and Facility Operation

The EM thruster was operated with a laboratory power processor unit (PPU) in conformity with the IAPS flight algorithms and standard operating conditions. Since the PPU has no automatic sequence capability, thruster transitions, e. g. from off to full beam (BF), were manually executed. All the thruster and diagnostics measurements were obtained under equilibrium, steady-state thruster operating conditions. Two minor differences between the ground test thruster operation with the PPU and the IAPS flight thruster subsystem operation were: (1) manual control of the beam current in the ground testing and (2) fixed-power neutralizer vaporizer operation in the ground testing.

The thruster cathodes were initially conditioned for 24 hr in the ground testing by a procedure similar to that employed in the flight test. Subsequent thruster operation included six startups to BF, 62 hr operation at BF, and 3.2 hr

operation in the steady state standby (SS) mode (with all thruster discharges but no high voltage on). Throughout the testing, the thruster starts and operation were smooth and nominal, with no arcs, recycles, or cathode extinctions.

Table II presents typical performance values of the EM thruster measured during BF operation. It also presents comparative values for one of the IAPS flight thrusters, obtained during a performance acceptance test. The propellant flowrates given for the EM thruster in the ground testing were measured with individual burettes over a period of several hours of BF operation at thermal equilibrium. Comparison of the EM ground correlation thruster performance with that of the flight thruster shows no significant differences except for a modestly higher discharge specific energy in the EM thruster. It is concluded that, for purposes of obtaining ground diagnostic measurements of thruster/spacecraft interactions, the thruster operation in the ground testing closely reproduced the IAPS flight thruster performance.

Visual observation following completion of the testing indicated that little backsputtered graphite from the beam target had deposited on the SMSS, the thruster, or any of the diagnostic instruments of the test apparatus. This result confirmed the low sputter yield and excellent performance of graphite as a beam target material for mercury thruster ground testing.

Deposition Measurements

QCM Results. The net deposition rates measured with the QCM at 25° C during thruster operation are presented in Table III. The rates were determined by the constant rates of increase (or decrease) of the beat frequency recorded on the strip chart recorder over substantial periods of steady-state thruster operation. Also presented in the table are typical values of the SCC potential (V_{S-G}) and the tank pressure during each measurement period. Most of the deposition rate measurements were obtained during BF thruster operation in configurations A and B, but rates were also determined during thruster operation in the SS mode and during the cathode conditioning at the beginning of the testing. The lower deposition rates observed under these latter conditions are consistent with the absence of the thruster beam and high voltage.

The two highly negative net deposition rates given in Table III were observed during BF thruster operation in configuration A while highly negative values of V_{S-G} prevailed. These V_{S-G} readings resulted from applied SPP bias voltages during SPP operation at elevated current levels, as subsequently described. The negative net deposition rates constitute ionic sputtering of existing deposits on the QCM detector crystal. The ions causing the sputtering are indicated to be principally Hg^+ charge exchange ions produced just downstream of the thruster grids.

The ICD measurements, subsequently discussed, indicate that most of the Hg^+ charge exchange ions left the thruster ion beam with ~30 eV energy. The ions were then accelerated as they approached the QCM by the ~120 V potential gradient created by the SCC potential, V_{S-P}, and struck the crystal with ~150 eV energy. This is well above the threshold energy for Hg^+ sputtering of any possible deposited material on the crystal. Hence the observed sputtering is expected.

Depositing Species. The only likely depositing materials which could be responsible for the observed positive BF deposition rates of Table III are: (1) molybdenum sputtered from the thruster accelerator grid by charge exchange ions and (2) carbon sputtered from the graphite beam target by the thruster primary ion beam. Mercury atoms or ions striking the detector crystal surface are not normally retained because of their volatility at the 25° C detector temperature and hence should not contribute significantly to the observed deposition. The sputtering noted at elevated V_{S-G} levels must therefore primarily be of deposited molybdenum or carbon (graphite). From reported yields for Hg^+ ion sputtering of these materials at 150 eV[7, 8], the flux of impinging ions may be calculated which is necessary to account for the observed net negative deposition rates. Such calculations have been made, taking into account the continued arrival of the depositing species during the observed sputtering periods.

The results of these calculations indicate that an impinging Hg^+ ion flux of 4.9×10^{11} ions cm^{-2} sec^{-1} (7.8×10^{-8} A cm^{-2}) is required if the sputtering is of molybdenum, whereas a flux of 7.3×10^{12} ions cm^{-2} sec^{-1} (1.2×10^{-6} A cm^{-2}) is required if the sputtered deposits were carbon. The much higher flux necessary in the latter case reflects the much lower yield of graphite than of molybdenum for Hg^+ ion sputtering. Only the Hg^+ ion flux level implied for molybdenum sputtering is consistent with Hg^+ charge exchange ion fluxes detected with the ICD's, as discussed in the following section.

The above sputtering calculations, together with other evidence discussed below, lead to the conclusion that molybdenum is the primary depositing species responsible for the QCM-observed deposition reported in Table III. The major source of the Mo is sputtering of the thruster accelerator grid by Hg^+ charge exchange ions. A secondary source is sputtering of the Mo coating on the beam shield interior surface by highly divergent, high energy Hg^+ ions from the thruster beam. The neutral Mo produced from both these sources has no line-of-sight view of the QCM, because the detector is totally shielded by the beam shield. Under the free molecular flow conditions prevailing in the ground testing, the observed deposition on the QCM must therefore be of Mo^+ ions, produced in the thruster beam by charge exchange of the neutral Mo from the above sources. The QCM data thus lead to the conclusion that ionic deposition predominates at the detector's beam-shielded location under the ground testing conditions.

The time-averaged deposition rate for all the BF configuration A data of Table III is 1.45 ng cm^{-2} hr^{-1}, not including the data at elevated V_{S-G} values. All of the averaged data were obtained at pressures < 1×10^{-4} Pa. The corresponding time-averaged deposition rate for the BF configuration B data in the table, again for pressures < 1×10^{-4} Pa, is 1.93 ng cm^{-2} hr^{-1}. The higher average deposition observed

in configuration B is consistent with the Mo^+ ionic deposition hypothesis, because of the effects of the different V_{S-G} values in the two configurations. In configuration A, the charge exchange Hg^+ ions impinging on the QCM at normal V_{S-G} voltages hit with ~40 eV energy. In configuration B their energy is ~8 eV lower because V_{S-G} is correspondingly higher. The sputter yield of Mo for Hg^+ ion bombardment is known[7] to depend very strongly on the ion energy in this range, and though the yields are low, they are sufficient to explain much of the difference between the average deposition rates found in the two configurations. If the QCM deposits were carbon, on the other hand, the sputter yields at the above Hg^+ ion bombardment energies would be so low as to have negligible effect on the net deposition rate observed in either configuration.

The variability of the positive BF deposition rates of Table III, in both configurations A and B, is believed to be associated with changes in the thruster ionic efflux distribution caused by altered experimental conditions. The variability of the measured rates is not primarily due to uncertainty in the individual rate determinations. The generally higher positive deposition rates observed in configuration B than in configuration A may correlate to some extent with the higher tank pressures during the former measurements (see Table III). However, higher accelerator drain currents were not observed at the higher pressures. Therefore, the Mo production by accelerator grid sputtering is not indicated to have been greater in configuration B than in configuration A.

The time-averaged deposition rate of 1.5 ng cm^{-2} hr^{-1} obtained from the QCM data taken during BF thruster operation in configuration A corresponds to a molybdenum thickness buildup of 0.15 nm per 100 hr of thruster operation at full beam. For the IAPS flight QCM's, with their lower sensitivity than the ground detector, such a deposition rate would cause the beat frequency to increase at the rate of 0.35 Hz hr^{-1}. Approximately 9 hr thruster operation at BF would be required to reach the estimated lower detection limit given in Table I for the flight QCM's, which corresponds to a 3 Hz change.

Vacuum Bakeouts. Prior to the initial thruster operation in the ground testing, hence before all of the QCM deposition measurements recorded in Table I, an anomalous hot shutdown of the vacuum tank caused a pressure rise from the normal operating vacuum to $> 10^{-1}$ Pa. After normal tank operation and vacuum were restored, the QCM beat frequency was found to be substantially higher. To remove volatile contaminants from the detector, it was baked out by raising its operating temperature to 100° C. After a total of 25 hr of vacuum bakeout the beat frequency had been lowered by > 400 Hz, and a final rate of decrease of ~1.5 Hz hr^{-1} at 100° C was achieved. At this point the thruster testing was begun.

During all the thruster operation in the ground testing, a total beat frequency increase of 58 Hz occurred (at 25° C), not including the small decrease noted at the end of the testing due to the brief period of deposit sputtering. Near the conclusion of the ground testing another vacuum bakeout of the QCM was performed at 100° C, for 9 hr. This lowered the beat frequency by 12 Hz (measured at 25° C). All of this decrease can be accounted for by continued removal of volatile contaminants, deposited on the detector crystal during the original hot shutdown of the tank, at the rate observed at the conclusion of the initial vacuum bakeout. The results of the final bakeout therefore strongly indicate that nearly all of the deposited material accumulated on the QCM during thruster operation was nonvolatile at 100° C in vacuum. This is fully consistent with the conclusion that the deposited material consisted predominantly of molybdenum.

DSH Results. The results of the deposition measurements made with the DSH's are presented in Table IV. The weight change uncertainty, as well as the lower detection limit for the weight changes, is estimated to be 2 µg. The agreement of the measured slide and mask weight gains for each detector is consistent with the approximately equal effective exposed area of each mask and slide.

On a mass-per-unit-area basis, the DSH slide and mask weight gains are much too large to be consistent with the deposition rates measured by the QCM. Further experiments will seek to resolve this discrepancy. Possible causes of it include: (1) anomalous deposition in the DSH's caused by their pre-test evacuation or by the multiple shutter actuations during the testing; (2) unidentified, specific facility or back-sputtering effects causing deposition in the DSH's substantially in excess of that received directly from the thruster, particularly in the case of DSH No. 2; and (3) the unknown floating potential of each DSH during the deposition periods, which could have caused ion focusing, defocusing, or sputtering at the DSH apertures and deposition surfaces. The much higher weight gains found with DSH No. 2 than with DSH No. 1 probably correlate with the slightly downstream aiming direction of the former, contrasted with the upstream aiming direction of the latter. (See Figs. 5(b) and 5(c).)

None of the DSH slide or mask deposits was visible. However, fairly uniform circular deposition stains were observed on the exteriors of both DSH shutters, conforming to the exposed area of each shutter in the open position. These stains were faint on the DSH No. 1 shutter and plainly evident on the DSH No. 2 shutter, roughly corresponding to the relative weight gains reported in Table IV for the two detectors.

Ion Efflux Measurements

ICD measurements of the thruster ion efflux were obtained in configurations A and B at BF to evaluate electron reflection by the shielding grid versus the applied voltage and to characterize the energy distribution of the detected ions by variation of the biasing grid potential. Comparison of the measurements obtained with the three identical detectors also permits evaluation of (1) the beam shield effectiveness in reducing the ion flux and (2) the variation of the ion flux with divergence angle, at angles near 90°.

Electron Penetration. Figure 9 presents typical data obtained in configuration A with ICD No. 3, which is the detector found to receive the highest ion flux during BF thruster operation. The plotted data assess the shielding grid effectiveness in reflecting electrons. In the figure, the measured currents reaching the collector plate, the shielding and suppressor grids, and the biasing grid are plotted vs. the shielding-suppressor grid voltage, V_{IS-G}, referred to tank ground. For all the measurements, the biasing grid voltage, V_{IB-S}, relative to SCC was constant at +25 V. Positive currents are net ion currents; negative currents are net electron currents. With the ambient plasma potential being very close to the tank ground potential, V_{IS-G} closely gives the effective shielding-suppressor grid potential, V_{IS-p}, as explained previously. The actual shielding-suppressor grid voltages, V_{IS-S}, set to obtain the data in Fig. 9 ranged from 0 to -21 V, measured from SCC.

From Fig. 9 it can be seen that the fixed IAPS value of -12V for V_{IS-S} was sufficient in configuration A to prevent essentially any electron penetration at the +25 V V_{IB-S} level. Nearly all incoming electrons were reflected at the shielding grid under these conditions, since lowering V_{IS-S} to -21 V did not increase the net ion current read at the collector plate or at any of the grids. As V_{IS-S} was raised from -12 to 0 V, increasing electron penetration occurred. In the Fig. 9 data this is seen from the fairly uniform decrements by which the electrons lowered the net ion currents measured at the collector plate and at all the grids, from the plateau currents measured at V_{IS-S} values of -12 V and lower. For V_{IS-S} = 0 V, a net electron current was observed at the biasing grid. The Fig. 9 results were typical for all three ICD's.

In configuration B, the data curves of Fig. 9 were fairly well reproduced. In this configuration, V_{IS-S} is equal to V_{IS-G}, since SCC is grounded to the tank. Hence, significant electron penetration did occur at V_{IS-S} = -12 V. However, this is not a flight configuration. In the flight configuration C, with the neutralizer switch closed, the effective shielding-suppressor grid potential is given by the sum of V_{IS-S} and V_C, the neutralizer coupling voltage. With $V_C \approx$ -12.5 V, from Table II, the IAPS value of -12 V for V_{IS-S} gives an effective shielding-suppressor grid potential of ~-24.5 V. Figure 9 shows that this potential should be totally effective in reflecting electrons, and no electron penetration should occur in this configuration under the given conditions.

At higher values of V_{IB-S} than the +25 V level of Fig. 9, the ICD data showed increasing electron penetration through the shielding and suppressor grids. At biasing grid potentials sufficient to reflect all charge exchange ions, net electron currents to the collector plate and biasing grid were readily observed in configuration A, even with V_{IS-S} = -12 V. Such currents were most prominent with ICD No. 1, less so with ICD No. 2, and least with ICD No. 3. This is the same as the order of increasing ion flux measured by the detectors. In the flight test, correction of the collector plate current data for electron penetration may be required for some of the ICD's

at the +96 V V_{IB-S} level, and possibly for a few of the detectors at the +55 V level. The magnitudes of the required corrections will be determined from the electron temperatures measured by the flight SPP and from the ground correlation measurements with the ICD's.

Ion Energy Distribution; Detector Characteristics. The energy distribution of the ion flux detected by ICD No. 3 during BF thruster operation in configuration A is presented in Fig. 10. This is a linear plot of the grid and collector plate currents measured as V_{IB-S} was varied from 0 to +96 V, with V_{IS-S} held at -12 V. The corresponding range of the plotted values of V_{IB-G} is from -9 to +87 V. The collector plate and biasing grid data both show the same simple ion energy distribution which was progressively cut off as V_{IB-G} was increased from +15 to +40 V.

If the peak ion energy of the Fig. 10 distributions is equated to the biasing grid potential at which the collector plate current was reduced to 20 percent of its maximum, this peak energy occurred for a V_{IB-S} value of ~+41 V. This is equivalent to a V_{IB-G} value of +32.2 V for the measured -8.8 V value of V_{S-G}, the SCC potential. As subsequently discussed, a value of -1.5 V was determined from the SPP data for V_{P-G}, the ambient plasma potential referred to tank ground. (The SPP data were taken under the same conditions as the Fig. 10 data.) This means that the peak energy of the detected ion distribution was ~33.7 eV in the ambient plasma, assuming singly charged ions.

The ion distribution depicted in Fig. 10 is clearly that of Hg^+ charge exchange ions generated in the central ion beam volume just downstream of the thruster grids. Such an ion distribution implies that plasma potentials of 16 to 41 V above the ambient plasma potential existed within the charge exchange ion production volume of the ion beam.

The data plotted in Fig. 10 display two other features of interest. The first is that a net electron current was collected on the biasing grid at all V_{IB-G} values above that necessary to reflect the bulk of the charge exchange ions. As previously explained, this electron current was due to electron penetration through the shielding grid. The effect slowly increased with V_{IB-G}, suggesting that the electron shielding barrier potential provided by the shielding grid was increasingly degraded as higher positive potentials were applied to the adjacent biasing grid. The second feature which may be noted in Fig. 10 is the rising net ion current collected by the shielding-suppressor grids as V_{IB-G} was increased above the level causing charge exchange ion reflection. This effect may be attributable to increasing collection of the reflected charge exchange ions on the shielding grid as V_{IB-G} was raised.

The ion energy distributions measured by the three ICD's during BF thruster operation in configuration A are compared in Fig. 11. This figure presents a semi-logarithmic plot of the measured collector plate currents for the three detectors as V_{IB-S} was varied from 0 to +96 V, corresponding to a V_{IB-G} range of -9 to +87 V for the

9

plotted data. V_{IS-S} was −12 V for all the data. Only positive, i. e., net collected ion currents are plotted. Despite the 100-fold range of the maximum collector plate current levels detected by the three ICD's, the plotted data for each of the detectors show the same basic charge exchange ion energy distribution. As previously found from Fig. 10, this distribution is cut off over the V_{IB-G} range from +15 to +40 V and has its peak energy at $V_{IB-G} \approx 32$ V. The residual high energy ion distribution shown by ICD No. 3 at V_{IB-G} values > +45 V in Fig. 11 was composed of high energy, highly divergent Hg^+ ions produced within the thruster grids.

The four fixed V_{IB-S} bias levels of the IAPS flight ICD's are indicated on Figs. 10 and 11. These were originally selected to permit biasing out the bulk of the detected charge exchange ions between the +25 and the +55 V levels. Figure 11 confirms that the two levels are appropriate to accomplish this for thruster operation in configuration A. They should also be proper in configuration C, with the neutralizer switch closed. In this case the detected charge exchange ion energy distributions of Fig. 11 will be uniformly shifted to V_{IB-G} levels ~4 V higher, because V_{S-G} will be lowered by this amount.

ICD Comparisons; Ion Trajectories and Total Fluxes. Table V is a compilation of data for all three ICD's, obtained during BF thruster operation in configuration A. The table gives measured and relative values of the detected grid and collector plate currents for the four flight biasing grid potentials. All of the data were obtained with V_{IS-S} at the −12 V flight value except for the first, reference case, in which V_{IS-S} was set at −21 V with V_{IB-S} at 0 V. This case is included to allow computation of total grid-plus-collector plate ion current values, I_{IT}, under conditions of maximum ion collection and minimum electron penetration/subtraction. All of the grid and collector plate ion currents measured for each detector in the five cases are given both as actual values and as computed percentages of the reference I_{IT} current value. Where net electron currents were detected at the higher V_{IB-S} levels, these are indicated as < 0 ion currents.

The Table V data reveal several important points.

(1) At both the 0 and +25 V V_{IB-S} levels (cases 1, 2, and 3), the grid and collector plate percentages of each detector's reference I_{IT} value were vastly different between the three detectors. Since the ion energy distribution seen by each ICD was about the same (from Fig. 11), this indicates that the trajectory distributions for the ions incident on the three detectors were very different. ICD No. 1 clearly received a highly nonnormally directed charge exchange ion flux, since its collector plate percentage of the total current was so low. This is consistent with the detector's shielded location in back of the beam shield and with the curved trajectories required for charge exchange ions to reach its collector plate. ICD No. 2 clearly received the most normally directed flux of charge exchange ions. Its collector plate current percentage was greater by a factor of about 3.5 than that of ICD

No. 1. This is consistent with the direct view and aiming of the detector into the charge exchange ion production volume. ICD No. 3 was intermediate to the other two detectors in its collector plate current percentage, and hence also in the inferred normality of the charge exchange ion flux incident on it.

(2) The best measure of the shielding of thruster ionic efflux provided by the beam shield is given by the ratios of the reference total ion current (I_{IT}) values for ICD's No. 1 and No. 2. This comparison indicates that the shield reduced the charge exchange ion flux in back of it (at the location of ICD No. 1) by a factor of ~2.5. If instead the ratio of collector plate currents of the two detectors were taken, an erroneously high shielding factor of ~9 would be inferred. Similarly, the ratio of the reference I_{IT} values for ICD's No. 2 and No. 3 gives a true factor of 13 for the higher charge exchange ion flux detected at ICD No. 3, compared with that at ICD No. 2. This ratio measures the strong dependence of the ion flux on the divergence angle from the thruster axis, as evaluated between the 81° angle of ICD No. 3 and the 104° angle of ICD No. 2. (See Fig. 5(b).)

(3) The first three cases show little real effect of changing V_{IS-S} from −12 to −21 V (at $V_{IB-S} = 0$ V) or of increasing V_{IB-S} from 0 V to +25 V (at $V_{IS-S} = -12$ V) for any of the detectors. These conclusions generalize the previous observations that negligible electron penetration occurred at the two lower IAPS V_{IB-S} levels with $V_{IS-S} = -12$ V and that nearly all the charge exchange ions detected had energies greater than the 17.7 eV cutoff value corresponding to the +25 V V_{IB-S} level. Though the conclusions were obtained for configuration A, they should apply as well for configuration C, with the neutralizer switch closed.

(4) As the V_{IB-S} level was increased to +96 V, the shielding-suppressor grid percentage of the reference I_{IT} value approached 50% for each of the detectors. For ICD's No. 2 and No. 3, the percentage was substantially lower at the lower V_{IB-S} levels. This observation suggests that when all the charge exchange ions entering a detector are either directly intercepted by the shielding grid or fully reflected by the biasing grid, the shielding grid will collect about half of the total number, regardless of the trajectory distribution of the incoming ions.

The reference I_{IT} values of Table V may be used to estimate the incident ion fluxes on each ICD, by taking the effective sensing area of each detector as the grounding grid area multiplied by the grid open area fraction. This accounts for the unmeasured interception of ions by the grounding grid. On this basis, the current densities indicated at the detector surfaces under the Table V conditions were 1.6×10^{-9}, 4.1×10^{-9}, and 5.5×10^{-8} A cm^{-2} for ICD's No. 1, 2, and 3, respectively. The corresponding ion fluxes thus were 1.0×10^{10}, 2.5×10^{10}, and 3.4×10^{11} ions cm^{-2} sec^{-1}, respectively, assuming singly charged ions.

ICD Responses to Thruster Startup Events. During the testing performed, it was observed that

10

the continuously recorded ICD collector plate cur-rents (with $V_{IB-S} = 0$ V) responded with varying sensitivity to all the major events in the stan-dard thruster startup sequence. Table VI lists the events causing observable ICD responses in a typical off-to-full beam startup in configuration B. The responses were generally of a sharp step-wise nature, either up or down. In a minority of cases, sharp transient responses were observed in which the ICD collector plate current immediately returned approximately to its previous level. The collector plate current responses were most promi-nent for ICD No. 3 and least prominent for ICD No. 1, paralleling the relative collector plate cur-rent levels of the detectors during BF thruster operation. By far the largest responses were observed when the thruster high voltage was turned on. This event normally caused a > 10-fold increase in the recorded collector plate current for each detector.

The ICD responses to startup events were observed for only a few thruster startups and were not definitively characterized. However, it is clear that ICD step-change responses will be observed in the flight test during thruster startups and other transitions. These responses will provide a valuable alternative means of moni-toring event occurrences and thruster performance during the commanded startups and transitions. Further ground correlation testing will establish standard ICD response signatures for the thruster startup events and will characterize the effects on these signatures of varying specific thruster operating conditions.

ICD Suitability for Flight Measurements. The ground test ICD data have demonstrated that reli-able collector plate ion current readings can be obtained down to about one percent of full scale on the 10^{-8} A range, well below the 10^{-9} A nominal lower limit of detector sensitivity indi-cated on Fig. 11. Thus the lower detection limit given in Table I for the ground ICD's corresponds to the collection of 1×10^{-10} A of ion current on the collector plate. The lower detection limit given for the flight ICD's is twice as high because of limitations in the telemetry of the collector plate current signals. The ground test-ing has confirmed that the sensitivity and stabil-ity of the flight detectors is more than adequate in the flight test to accurately characterize the ion flux at each ICD location during operation of the adjacent ion thruster.

The flight ICD sensitivity is also fully adequate to measure the environmental ram ion flux seen by the flight detector corresponding to ICD No. 3, when the spacecraft +X axis coincides with the spacecraft velocity vector (as depicted in Fig. 1). A collector plate ion current of $\sim 1.0 \times 10^{-7}$ A is expected under these condi-tions, with neither thruster in operation. This value is calculated from an environmental ion den-sity of 2.7×10^4 cm^{-3} [9] and a spacecraft velocity of 7.48 km sec^{-1} at the 740 km orbital altitude.

The highest ICD collector plate current levels detected in the ground testing were $\sim 1.4 \times 10^{-6}$ A, a level briefly measured by ICD No. 3 during BF thruster operation. This is 0.14 percent of the detector's upper measurement limit

of 1.0×10^{-3} A. Higher currents are expected to be observed when testing is performed with an ICD in the inboard detector mount seen in Fig. 5(b). Any higher current levels measured, however, will certainly not approach the upper measurement limit. The ground testing results thus substanti-ate the ICD design, performance, and detection limits (both upper and lower) as being very ade-quate and well suited to acquiring the ion flux measurements required of the seven detectors in the flight test.

Plasma Electron Current and Potential Measurements

SPP Data and Plotting. The current-voltage measurements taken with the SPP in the ground testing characterized the probe voltages required for collection of fixed electron currents from the thruster-generated plasma. The probe data also have been analyzed to characterize the potential and other properties of the ambient plasma. Data were taken during BF thruster operation in con-figurations A and B and during SS operation in configuration B. Comparative analysis indicates that the current-voltage relationship for electron collection on the probe was basically the same in both configurations. Comparison of data obtained during voltage-controlled operation with that obtained during current-controlled operation of the probe also showed general agreement, except for minor anomalies at the lowest current levels.

The measured SPP current-voltage data obtained during steady state BF thruster operation in configuration A are presented in Table VII. For each flight SPP current level, the table gives the measured current (I_{PP}), voltage (V_{PP-S}) from SCC, and SCC potential (V_{S-G}) from tank ground. The final column of the table gives the calculated SPP potential (V_{PP-G}) from tank ground for each current level, as obtained from the sum of V_{PP-S} and V_{S-G}. The I_{PP} data are plotted semi-logarithmically against the corre-sponding calculated V_{PP-G} values in Fig. 12, with a small constant correction of 1.21 μA added to each current value. This correction, which is subsequently explained, represents the estimated ion current collected on the probe during each of the measurements. Each plotted current therefore represents the total electron current collected on the probe.

Loading down of the current-reading electro-meter caused erroneous I_{PP} readings at current levels 15 and 16 in the Table VII and Fig. 12 data, without affecting the corresponding voltage readings. Prior unloaded calibration readings of the currents at these levels are assumed correct for the thruster-on measurements, however. These are given in the table and plotted as the cor-rected data points in Fig. 12.

Langmuir Curve Analysis. Besides showing the variation of the SPP-collected electron current with applied bias potential, the plotted data in Fig. 12 form a Langmuir curve with a compound electron-retarding branch. The data were analyzed by standard techniques such as given in Ref. 10. This analysis is presented on the figure. The principal conclusions from the analysis, and from comparison of the data with corresponding SPP data obtained in configuration B, are the following:

(1) The ambient plasma potential in configuration A during BF thruster operation was 7.2 $\pm$ 1 V above the floating SCC potential, measured to be 8.7 V below tank ground. Thus, the plasma potential was 1.5 $\pm$ 1 V below tank ground. This small potential difference may be explained by secondary electron emission from impingement of the primary ion beam on the grounded beam target. The comparable plasma potential derived from the configuration B SPP data taken during BF thruster operation was found to be 0 $\pm$ 1 V, referenced to tank ground. In this configuration, secondary electron emission effects are negated by the grounding of SCC to the tank.

(2) Maxwellian electron groups with temperatures of $\sim$0.84 and 3.15 eV were distinctly resolved in the electron-retarding portion of the configuration A data, as shown in Fig. 12. To accomplish this, the fitted line representing the high energy distribution was subtracted from the total current data. The line representing the low energy distribution was then fitted to the residual currents, which are plotted on the figure. Analysis of comparable SPP data obtained in configuration B gave a composite temperature of 1.40 eV for the electrons. The plot of the configuration B data showed the high energy electron group to be substantially reduced from that seen in Fig. 12. As a result, it could not be distinctly resolved from the low energy group. Limited SPP data obtained during SS thruster operation in configuration B gave an electron temperature of $\sim$1.25 eV under these conditions. The differences found between the configuration A and B SPP electron collection data during BF thruster operation may be attributable to effects of the different SCC potentials on the neutralizer emission in the two configurations.

(3) The ambient plasma density at the SPP in configuration A, estimated from the data curve analysis shown in Fig. 12, was 4.9×10^5 cm^{-3}. This estimate assumes that the -1.5 V plasma potential obtained from the same analysis is correct. The density determination is subject to a large uncertainty as a consequence of both the incomplete definition of the electron saturation branch of the data plot and the two electron distributions found in the retarding branch data.

(4) Iterative analysis of the Fig. 12 data gave a best fit value of 1.21 μA for the electron current collected by the SPP at its measured floating potential of -14.78 V (referenced to tank ground). This current level is shown on the figure at the floating potential and falls on the 3.15 eV electron distribution line. It implies that an equivalent random ion current of the same magnitude was collected by the probe at this potential. Since the ICD data established that most of the ions had > 25 eV energy (at plasma potential), it may be assumed that this same level of random ion current was collected by the probe at all SPP voltages over the range tested. Hence, the measured Ipp values were corrected by this amount to obtain the total collected electron currents plotted in Fig. 12. A value of 1.2 μA for the random ion current impinging on the SPP is consistent with a value of 1.9 μA independently estimated by assuming the total ion current density determined by ICD No. 2 intercepted the SPP cross sectional area of 461 cm^2. The random ion

current to the SPP sphere could have been measured directly if the probe had been biased to potentials below the floating potential.

The configuration A and B SPP data at BF were taken over a range of tank pressures extending from 5 to 16×10^{-5} Pa. The tank pressure was found to correlate with changes observed in the SPP bias voltages read for current levels in the electron saturation branch region. This correlation agreed with the expected increase in the plasma density with pressure.

Balancing Ion Collection; Effect on SCC Potential. Figure 13 presents a semi-logarithmic plot of the balancing ion currents collected on SCC, as a function of the SCC potential, for the configuration A SPP data of Fig. 12. These ion currents, which are equivalent to the Ipp values in Table VII, are plotted vs. the measured V_{S-G} values given in the table. As noted previously, SCC acts as a second probe during SPP operation in configuration A, and the V_{S-G} values observed give for each current level the negative potential necessary for collection on SCC of a net ion current equivalent to the net electron current collected on the SPP sphere. (As in Fig. 12, corrected current values are shown on Fig. 13 for SPP current levels 15 and 16.)

In Fig. 13 it is seen that operation of the SPP in configuration A at current levels above 49 μA (level 8) rapidly drove the SCC potential negative, relative to tank ground. At 477 μA collected current (level 12), V_{S-G} was -117 V, and it approached its lowest value of -124 V at higher collected current levels (> 1.51 mA). The V_{S-G} plateau observed at ~ -124 V was not the consequence of any clamping diode action. A possible explanation of it is that the plasma sheath adjoining the thruster ground screen mask grew with increasing $|V_{S-G}|$ to a critical depth sufficient to extract any required level of ion current from the high density fringe of the ion beam. The ground screen mask is indicated to be the principal SCC-potential surface collecting the balancing ion current. The plasma sheath thickness on it may be calculated for space charge-limited ion collection. Assuming uniform collection of all the balancing ion current on the ground screen mask, the sheath thickness reached 2.1 cm at the higher SPP current/voltage levels. This was sufficient to substantially infringe on the ion beam passing through the mask opening. Also possibly contributing to the occurrence of the observed plateau in V_{S-G} was the onset or sharp increase, at this voltage, in the secondary electron emission arising from the impingement of the collected ions on the SCC surfaces.

SPP Suitability for Flight Measurements. The SPP data obtained in both configurations A and B support the validity of applying standard Langmuir probe analysis procedures to the SPP data in order to determine the SCC potential in the flight test. The flight SPP data obtained with the neutralizer switch closed (configuration C) will characterize the probe electron collection variation with bias voltage and the ambient plasma properties. The latter include definition of the SCC potential (referenced to the ambient space plasma), the electron temperature(s), and the ambient plasma density at the probe. Comparative

flight SPP data taken with the neutralizer switch open (configuration A) will then characterize the ion current collection on all the IAPS and spacecraft surfaces at SCC potential, by giving the SCC potential variation with the SPP current level. Based on the ground test results, the electron current collection on the SPP should identically depend on the probe-to-ambient plasma voltage difference whether the neutralizer switch is open or closed.

The ground test SPP data plotted in Fig. 12 illustrate the importance of (1) the multiple SPP current level setpoints at logarithmic intervals and (2) the large probe area, which gives it a high electron saturation current. As seen in the figure, these features permit the electron-retarding branch of the Langmuir curve generated by the probe data to be accurately defined. This in turn enables resolution of multiple Maxwellian electron groups in the retarding branch and determination of their individual temperatures. In the flight test the SPP is expected to detect an additional Maxwellian group, namely, the ~0.3 eV ambient electrons of the orbital environment. This will make the above probe design features even more important, because three electron groups may have to be resolved in order to fully interpret the probe data.

The ground test results obtained to date with the SPP confirm that its design, current-controlled operation, setpoint range and intervals, and location are appropriate for the flight test. All of these factors will facilitate acquiring the interaction measurements required during the flight thruster operation.

Floating Potential Measurements and Calculated Values

The floating potentials of SCC, the SPP, and the beam shield were measured during the ground testing. The values obtained during BF thruster operation in configurations A and B are presented in the first data column of Table VIII, as referenced to tank ground. The second data column gives the corresponding values referenced to the ambient plasma potential, based on the plasma potential determinations made from the SPP data. The measured floating potentials were in general reproducible to ± 0.1 V or better.

Two distinct values for the SPP floating potential in configuration A were observed at different times during the testing, as shown in the table, with the -14.8 V value observed more frequently. Intermediate values were not observed. From Fig. 12 and the calculations described below, it may be concluded that the -14.8 V value was due to the presence of the high energy, 3.15 eV electron group seen in the figure and the -7.9 V value was due to the absence of this group. (Note in Fig. 12 that the extrapolated SPP voltage for the 0.84 eV electron group alone at the 1.2 µA balancing ion current level is ~-7.8 V.) Further investigation is required to understand why the high energy electron group appeared and disappeared in the SPP data.

Calculated floating potential values for the structures and components of the experimental apparatus may be obtained for BF operation by

iteratively solving the equation (simplified from Ref. 9):

$$\phi = -\frac{kT_e}{e} \ln \frac{\left(\frac{8kT_e}{\pi}\right)^{1/2} \left(\frac{m_i}{m_e}\right)^{1/2}}{\left(\frac{8kT_i}{\pi} + m_i v_i^2\right)^{1/2} - \frac{2e\phi}{\left(\frac{8kT_i}{\pi} + m_i v_i^2\right)^{1/2}}} \tag{1}$$

In equation (1), ϕ is the floating potential (referenced to the plasma potential), T_e and T_i are the electron and ion temperatures, m_e and m_i are the electron and ion masses, v_i is the ion drift velocity, k is Boltzmann's constant, and e is the electronic charge.

Predicted floating potentials have been calculated with equation (1), on the assumptions that the ions present are all Hg^+ ions having a Maxwellian temperature of 550 K (the approximate accelerator grid temperature) and a drift velocity given by the 33.7 eV peak energy measured by the ICD's in configuration A. The SPP floating potentials thus calculated are given in the third data column of Table VIII for each of the electron temperatures shown in the fourth data column. These electron temperatures are the values obtained from analyzing the SPP data. The calculated floating potentials are referenced to the ambient plasma potential and may be compared with the values given in the second data column of the table. It will be found in general from equation (1) that, over the accessible ranges of the variables, the magnitude of the predicted floating potential monotonically increases with the electron temperature.

Conversely, equation (1) may be used to calculate the electron temperatures required to produce the observed floating potentials. This has been done, and the resulting temperatures are given in the fifth data column of Table VIII.

Examination of the measured and calculated floating potentials and electron temperatures in Table VIII leads to several conclusions.

(1) Semi-quantitative agreement is found between the electron temperatures extracted from the SPP data, the ion energies measured by the ICD's, and the measured floating potentials, using equation (1).

(2) All the measured and calculated floating potentials are negative, relative to the ambient plasma potential, and all are attributable to the high energy electrons present at the plasma potential in the identified Maxwellian electron groups. The negative floating potentials do not infer the presence or detection of electrons at potentials below the ambient plasma potential, though such negative potentials could have occurred in the immediate vicinity of the neutralizer.

(3) The high temperature (3.15 eV) electron group seen in the configuration A SPP data (Fig.

12) was only found to control the floating potential of the SPP. Further, the occasional, unexplained disappearance of this electron group resulted in the probe floating potential being controlled by the observed low temperature electron group.

(4) As calculated from the floating potentials measured in configuration A, the effective electron temperatures at the SCC surfaces, the beam shield, and the SPP decreased in the order given, if the smaller of the two observed SPP floating potentials is considered. This is also the order of decreasing proximity of these components or surfaces to the neutralizer, taking the principal SCC surface as the ground screen mask. Such a correlation suggests that partial cooling or thermalization of initially hotter electrons emitted by the neutralizer took place as the electrons diffused to surfaces farther and farther away. It also suggests that the neutralizer emitted both the high and the low temperature electron groups seen in the SPP data, with the high temperature electrons not observed elsewhere than at the SPP.

Summary and Conclusions

A preliminary ground correlation investigation has been conducted of the thruster/spacecraft interactions to be measured on the IAPS flight test. The thruster, diagnostic instrumentation, and experimental configuration (both mechanical and electrical) closely replicated the corresponding flight hardware and configuration.

The ground test data form a data base which is expected to accurately correlate with and facilitate interpretation of the flight test interaction measurements. The test data acquired have verified that the comparable flight detectors are adequate for fully achieving the interaction evaluation required in order to accomplish the flight test objective. Not just the design, but also the operation and configuration of the detectors have been confirmed.

The ground test data have revealed the critical effect of the spacecraft potential on the measured interactions and on the detector operation. The data have evaluated the depositional and electrical interactions of the 8 cm IAPS mercury thruster subsystem with spacecraft surfaces, including assessment of the protection provided by the thruster beam shield. The preliminary results obtained support the compatibility of the IAPS thrusters with host spacecraft in auxiliary propulsion applications, particularly north-south stationkeeping.

The principal specific results and conclusions reported in this paper from the ground test investigation are the following:

(1) The SCC potential has a first order effect on all the thruster/spacecraft interactions to be measured during the IAPS flight test or on the diagnostic measurements of these interactions. This is true of both the depositional and the electrical interactions investigated. Each diagnostic measurement must be obtained with the SCC potential known and held constant.

(2) Realistic ground correlation measurements of thruster/spacecraft interactions must be carried out with an electrical configuration closely reproducing the flight configuration. In particular, the thruster power processor and all flight-type diagnostic instruments must be referenced to a common, floating ground (SCC), which is totally isolated from the test facility ground and all other instrumentation. The flight surfaces at the SCC potential must also be reproduced.

(3) The SPP current level setpoints and the neutralizer switch position provide limited control of the SCC potential during BF thruster operation. This control is over the range from approximately -8 to -120 V, relative to the ambient plasma potential.

(4) Nonvolatile thruster efflux was found to deposit on the high boom QCM at a net rate of ~ 1.5 ng cm^{-2} per hour of BF thruster operation in configuration A, with the detector maintained at 25° C. Rapid sputter removal of the QCM deposits was observed when very negative SCC potentials caused > 100 eV acceleration of the impinging ionic species (indicated to be mainly Hg^+). Because of the observed sputter removal rate and the nonvolatility at 100° C of the deposits, they are concluded to consist mainly of molybdenum sputtered from the thruster accelerator grid. Since the QCM had no line-of-sight view of the accelerator grid, the retained deposition is inferred to have arrived at the detector as Mo^+ ions formed by charge exchange in the thruster ion beam.

(5) The ICD measurements during BF thruster operation show that the thruster ionic efflux detected at high divergence angles consisted almost totally of 20 to 34 eV charge exchange ions. The three detectors measured the same energy spectrum but very different current densities and trajectory distributions for the incident ions.

(6) The ICD measurements upstream of the thruster grid plane indicate that the beam shield reduced the total thruster-generated ion flux by a factor of ~ 2.5 during BF operation. The ICD measurements also show that the ion flux decreased rapidly with increasing divergence angle from the thruster axis.

(7) The ICD current collection ranges and lower detection limit ($\sim 10^{-10}$ A) fully accommodate and are well suited to the required detector measurements during thruster operation in the flight test. The flight biasing grid voltage setpoints are at proper levels to discriminate environmental, normal charge exchange, and high energy divergent beam ions. The fixed flight level of the shielding-suppressor grid voltage is adequate to prevent significant electron penetration at all but the highest biasing grid voltages. The ICD's sensitively respond to and track normal thruster startup events, with their strongest response found to be a tenfold collected current increase at turnon of the thruster high voltage.

(8) During BF thruster operation, the SPP collected total electron currents from 3 μA to 5 mA over a bias voltage range from -10 to +22 V relative to the ambient plasma potential.

14

(9) The SPP current-voltage data at the 16 flight detector current levels generate a Langmuir curve from which the SCC-to-ambient plasma potential difference is readily determined. This difference gives the SCC potential in the flight test. A compound electron-retarding branch was found in the Langmuir curve obtained from the SPP data taken during BF thruster operation in configuration A. This was resolved to indicate the presence of two Maxwellian electron groups, having temperatures of ~3.15 and 0.84 eV.

(10) SPP operation at its higher current collection levels during BF thruster operation in configuration A drove the SCC potential very negative, to a plateau voltage ~122 V below the ambient plasma potential. This phenomenom was due to the detector circuit requirement that the SCC surfaces collect a net ion current balancing the net electron current received by the SPP sphere. The ion collection requirement is removed when the neutralizer switch is closed. In order to fully interpret the SPP interaction measurements during the flight test, comparative probe data must be taken with the neutralizer switch open and closed.

(11) The SPP large-area design, current-controlled operation, setpoint range and levels, and detector location are well suited to obtaining the required flight test diagnostic measurements of electron current collection, spacecraft potential, and ambient plasma properties.

(12) The SCC and the thruster beam shield were found to electrically float at 7.2 and 6.6 V below the ambient plasma potential, respectively, during BF thruster operation in configuration A. These values were 5.4 and 6.0 V, respectively, above the neutralizer emitting potential. The floating potentials were very reproducible and imply control by 1.3 to 1.5 eV electrons emitted from the neutralizer. The SPP exhibited two floating potentials in semi-quantitative agreement with the two electron temperatures analyzed from the probe data. The observed two floating potentials are explained by the appearance and disappearance of the high temperature electron group detected by the probe.

References

1. Power, J. L., "Planned Flight Test of a Mercury Ion Auxiliary Propulsion System. I - Objectives, Systems Descriptions, and Mission Operations," NASA TM-78859, 1978.

2. Power, J. L., "Measuring the Spacecraft and Environmental Interactions of the 8-cm Mercury Ion Thrusters on the P80-1 Mission," Electric Propulsion and Its Applications to Space Missions, edited by R. C. Finke, AIAA, New York, 1981, pp. 813-825.

3. Hurst, E. B., and Thomas, G. Z., "Diagnostic System Design for the Ion Auxiliary Propulsion System (IAPS) - Flight Test of Two 8-cm Mercury Ion Thrusters," AIAA Paper 81-0666, Apr. 1981.

4. Byers, D. C., "A Review of Electron Bombardment Thruster Systems/Spacecraft Field and Particle Interfaces," NASA TM-78850, 1978.

5. Kaufman, H. R., and Carruth, M. R., "Charge-Exchange Plasma Environment for an Ion Drive Spacecraft," JPL Publication 79-90, 1979.

6. Weigand, A. J., and Mirtich, M. J., "Change in Transmittance of Fused Silica as a Means of Detecting Material Sputtered from Components on a 5-cm Ion Thruster," NASA TM X-68073, 1972.

7. Askerov, Sh. G., and Sena, L. A., "Cathode Sputtering of Metals by Slow Mercury Ions," Fizika Tverdogo Tela Vol. 11, No. 6, June 1969, pp. 1591-1597; English translation: Soviet Physics - Solid State Vol. 11, No. 6, Dec. 1969, pp. 1288-1293.

8. Wehner, G. K., "Sputtering Yields for Normally Incident Hg^+ - Ion Bombardment at Low Ion Energy," Physical Review Vol. 108, No. 1, Oct. 1, 1957, pp. 35-45.

9. Anon.: "The Earth's Ionosphere," NASA SP-8049, 1971.

10. Bell, R. B., "An Experimental Study of Cylindrical Langmuir Probes in a Collisionless Quiescent Argon Glow Discharge," M. S. Thesis, Air Force Institute of Technology, Wright-Patterson Air Force Base, June 1968; also published as Report GSP/PH/68-1.

TABLE I. - THRUSTER/SPACECRAFT INTERACTIONS MEASURED IN FLIGHT AND GROUND TESTING

Interaction	Diagnostic instruments	No. of detectors		Measurement/Determination	Estimated lower detection limit
		Flight	Ground		
DEPOSITIONAL					
Deposition retained at 25° C (e.g., Mo)	QCM	2	1	Beat frequency increase	Flight: 13 ng cm^{-2} Ground: 1.5 ng cm^{-2}
	Warm SCM	5	0	Short circuit output current decrease	Flight: 300 ng cm^{-2}
	DSH	0	2	Slide and mask weight gain	Ground: Under investigation
Deposition retained on cold (≤-60° C) surfaces (e.g., Hg)	Cold SCM	4	0	Short circuit output current decrease	Flight: 400 ng cm^{-2}
	Cold SCM Radiator	4	0	Cooling performance degradation	Flight: 150 ng cm^{-2}
ELECTRICAL					
Ion fluxes to spacecraft surfaces	ICD	7	3	Collector plate current (and grid currents for ground detectors)	Flight: 6.3x10^{-12} A cm^{-2} Ground: 3.2x10^{-12} A cm^{-2}
Electron currents to biased space-craft surfaces	SPP	1	1	Bias voltage for selected current level	Flight and Ground: 5.5x10^{-10} A cm^{-2}
Spacecraft potential (from ambient plasma potential)	SPP	Above	Above	Langmuir curve analysis of bias voltage vs. current data	Flight and Ground: -205 V

TABLE II. - GROUND/FLIGHT THRUSTER PERFORMANCE COMPARISON[a]

Parameter	Symbol	Determined from	Units	Ground test thruster	Flight thruster
Screen voltage	V_S		V	1180	1180
Beam voltage	V_B	$V_S + V_D - \|V_C\|$	V	1207	1207
Beam current	I_S		mA	72.0	72
Beam power	P_B	$V_B I_S$	W	86.9	86.9
Accelerator voltage	V_A		V	-301	-297
Accelerator current	I_A		μA	241	272
Discharge voltage	V_D		V	39.1	39.0
Keeper-to-anode voltage	V_δ	$V_D - V_{DK}$	V	25.9	26.0
Discharge current[b]	I_D		mA	486	448
Discharge keeper voltage	V_{DK}		V	13.2	13.0
Discharge keeper current	I_{DK}		mA	61	60
Discharge tip heater power	P_{DH}		W	2.4	3.0
Discharge vaporizer power	P_{DV}		W	6.4	7.2
Discharge vaporizer flowrate	$\dot{m}_D$		mA[c]	98.1	95.4
Neutralizer keeper voltage	V_{NK}		V	16.4	16.1
Neutralizer keeper current	I_{NK}		mA	497	500
Neutralizer tip heater power	P_{NH}		W	3.9	3.8
Neutralizer vaporizer power	P_{NV}		W	1.4	1.8
Neutralizer vaporizer flowrate	$\dot{m}_N$		mA[c]	3.8	6.0
Neutralizer coupling voltage	V_C		V	-12.6	-12.4
Total thruster input power	P_T	$\sum$ (All power terms[d])	W	129.9	130.0
Total propellant flowrate	$\dot{m}_T$	$\dot{m}_D + \dot{m}_N$	mA[c]	102.0	101.4
Electrical efficiency	η_E	P_B/P_T	(%)	66.9	66.8
Discharge propellant efficiency	η_{PD}	$I_S/\dot{m}_D$	(%)	73.4	75.5
Total propellant efficiency	η_{PT}	$I_S/\dot{m}_T$	(%)	70.6	71.0
Thrust	T	$0.002039\ I_S V_B^{1/2}$	mN	5.10	5.10
Specific impulse	I_{SP}	$100.02\ \eta_{PT} V_B^{1/2}$	sec	2453	2467
Discharge specific energy	ϵ	$(V_D I_D + V_{DK} I_{DK})/I_S$	eV/ion	275	253

[a]Uncorrected for small effects of beam divergence and Hg^{+2} ion production.
[b]Not including beam current.
[c]Equivalent. Conversion to mass flowrate: 1 mA = 7.48 mg hr^{-1} for Hg.
[d]Power terms included: $V_S I_S$, $\|V_A\| I_A$, $V_D(I_D + I_S)$, $V_{DK} I_{DK}$, $V_{NK} I_{NK}$, P_{DH}, P_{NH}, P_{DV}, and P_{NV}.

TABLE III. - DEPOSITION RATES MEASURED BY QCM AT 25.0° C

Thruster mode	Configuration	V_{S-G} (typical), V	Tank pressure, Pa	Time period, hr	Deposition rate	
					Hz/hr.	[a] ng cm^{-2} hr^{-1}
BF	A	-8.7	7×10^{-5}	9.6	0.71	1.11
		-8.3		2.6	.73	1.14
		-8.8		7.7	1.11	1.73
		-8.4		5.5	1.15	1.79
		-119.9[b]		.44	-9.1	-14.2
		-123.5[b]		.17	-9.9	-15.5
BF	B	0		1.9	1.03	1.60
			8×10^{-5}	7.1	1.09	1.70
			1.8×10^{-4}	5.2	1.17	1.82
			8×10^{-5}	3.9	1.46	2.27
			9×10^{-5}	1.7	1.56	2.44
			1.4×10^{-4}	1.0	2.00	3.12
SS[c]	B		1.3×10^{-4}	3.4	.28	.44
CC[c,d]	B		1.1×10^{-4}	1.9	.49	.76

[a] Determined from measured Hz/hr rate by conversion factor of 1 Hz = 1.56 ng cm^{-2} (for 15 MHz crystals employed).

[b] Highly negative value caused by SPP operation at high current level.

[c] Beam off.

[d] Cathode conditioning. Same as SS but with reduced $\dot{m}_D$ and increased P_{DH} and P_{NH}.

TABLE IV. - DEPOSITION MEASURED BY

DEPOSITION SLIDE HOLDERS

AT 25° C

DSH number	Location	Total shutter-open time,[a] hr	Weight change, µg	
			Slide	Mask
1	High boom	33.18	+4	+5
2	SMSS deck	33.13	+28	+27

[a] Thruster always in nominal full beam operation.

TABLE V. - MEASURED, RELATIVE, AND TOTAL ION CURRENTS OF ICD's DURING

BF THRUSTER OPERATION IN CONFIGURATION A

Case number		1		2		3		4		5	
V_{IB-S}, V		0		0		+25		+55		+96	
V_{IS-S}, V		-21		-12		-12		-12		-12	
ICD number	Parameter	Value	% of Case 1 I_{IT}	Value	% of Case 1 I_{IT}	Value	% of Case 1 I_{IT}	Value	% of Case 1 I_{IT}	Value	% of Case 1 I_{IT}
All	V_{S-G}, V	-8.7	-----	-8.8	---	-8.8	---	-8.7	-----	-8.7	-----
	V_{IB-G}, V	-8.7	-----	-8.8	---	+16.2	---	+46.3	-----	+87.3	-----
	V_{IS-G}, V	-29.7	-----	-20.8	---	-20.8	---	-20.7	-----	-20.7	-----
1	I_{IC}, µA	0.013	22	0.014	23	0.010	17	<0	-----	<0	-----
	I_{IB}, µA	.015	25	.015	25	.0062	10	<0	-----	<0	-----
	I_{IS}, µA	.032	53	.030	49	.034	56	.032	54	.032	54
	$\sum = I_{IT}$, µA	.060	100	.059	97	.050	83	--------	-----	-------	-----
2	I_{IC}, µA	0.119	78	0.113	74	0.096	63	0.00049	0.32	<0	-----
	I_{IB}, µA	.021	14	.022	14	.027	17	<0	<0	<0	-----
	I_{IS}, µA	.012	7.9	.019	12	.016	11	.046	30	.065	43
	$\sum = I_{IT}$, µA	.152	100	.153	101	.139	91	--------	-----	-------	-----
3	I_{IC}, µA	0.963	47	0.899	44	0.898	44	0.010	0.49	0.0044	0.21
	I_{IB}, µA	.401	20	.390	19	.255	12	<0	-----	<0	-----
	I_{IS}, µA	.679	33	.693	34	.577	28	.799	39	.965	47
	$\sum = I_{IT}$, µA	2.04	100	1.98	97	1.73	85	--------	-----	-------	-----

Negative current values signify net electron collection.

TABLE VI. - THRUSTER STARTUP EVENTS CAUSING OBSERVABLE

ICD RESPONSES - CONFIGURATION B

Events in normal chronological order of occurrence[a]:
1. Discharge cathode ignition.
2. Main discharge ignition.
3. I_D increase to 700 mA.
4. Neutralizer ignition.
5. I_D cutback to 350 mA.
6. I_{QK} increase to 360 mA (preparatory to high voltage turnon).
7. High voltage turnon.
8. Rampup of I_S, via I_D, to full beam.
9. Discharge vaporizer flow increase, via control loop.
10. Discharge vaporizer flow decrease, via control loop.

[a]Event number 4 may occur any time up to event number 6.

TABLE VII. - SPP DATA WITH THRUSTER AT FULL BEAM - CONFIGURATION A

I_{pp} level[a] number	Measured I_{pp},[b] μA	Measured V_{pp-s}, V	Measured V_{s-G}, V	Calculated V_{pp-G},[c] V
Floating	0.0	-6.09	-8.69	-14.78
1	2.16[d]	-2.95	-8.74	-11.69
2	2.58[e]	-2.89	-8.76	-11.65
3	2.87	-2.30	-8.73	-11.03
4	5.12	-1.155	-8.80	-9.96
5	8.95	+.960	-8.91	-7.95
6	16.02	+2.38	-9.10	-6.72
7	28.4	+3.55	-9.52	-5.97
8	49.4	+5.01	-10.36	-5.35
9	88.3	+8.39	-12.88	-4.49
10	155.7	+32.6	-36.0	-3.4
11	276	+85.9	-87.5	-1.6
12	477	+118.0	-117.3	+0.7
13	854	+122.8	-119.9	+2.9
14	1511	+128.9	-122.6	+6.3
15	2650[f]	+135.0	-123.3	+11.7
16	4679[f]	+144.2	-123.5	+20.7

[a]Same level number and nominal I_{pp} as IAPS flight SPP.

[b]Net electron current collected on probe; also net ion current collected on SCC.

[c]Equals $V_{pp-s} + V_{s-G}$.

[d]Nominal value is 0.94 μA.

[e]Nominal value is 1.63 μA.

[f]Corrected value from dummy load calibration. Measured value reduced due to electrometer loading.

TABLE VIII. - MEASURED/CALCULATED STRUCTURAL FLOATING POTENTIALS AND

PLASMA ELECTRON TEMPERATURES WITH THRUSTER AT FULL BEAM

Structure/Component	Config-uration	Measured floating potential, from tank ground, V	Floating potential, from plasma potential,[a] V	Calculated floating potential, from plasma potential, V	Electron temperature-SPP data, eV	Calculated electron temperature-based on measured floating potential, eV
SPP	A	-14.8^b	-13.3	-15.6	3.15	2.69
		-7.9^b	-6.4	-3.8	0.84	1.35
	B	-7.4	-7.4	-6.7	1.40^c	1.54
Beam	A	-8.1	-6.6	-----	-----	1.39
Shield	B	-7.8	-7.8	-----	-----	1.62
SCC	A	-8.7	-7.2	-----	-----	1.53
	B	0	0	-----	-----	----

[a]Plasma potentials determined from SPP data; = -1.5 V in configuration A and

0 V in configuration B.

[b]Two values observed.
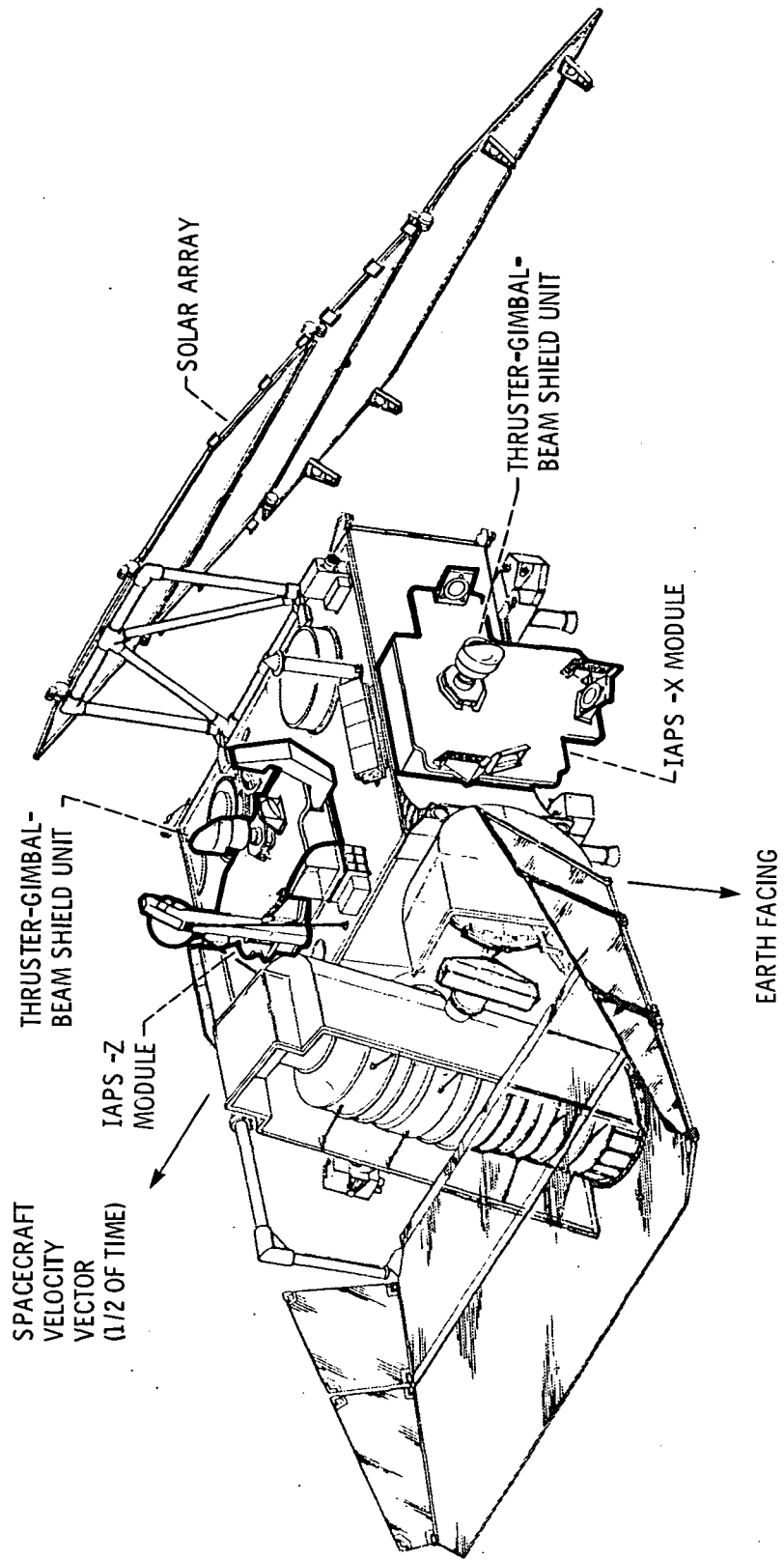
[c]Composite value - see text.

SOLAR ARRAY

THRUSTER-GIMBAL-
BEAM SHIELD UNIT

THRUSTER-GIMBAL-
BEAM SHIELD UNIT

IAPS -X MODULE

IAPS -Z
MODULE

SPACECRAFT
VELOCITY
VECTOR
(1/2 OF TIME)

EARTH FACING

Fig. 1. – Spacecraft with IAPS modules.

WARM SOLAR
CELL MONITORS

QUARTZ CRYSTAL
MICROBALANCE

RADIATOR

SPACECRAFT
POTENTIAL
PROBE

COLD SOLAR
CELL MONITOR

ION COLLECTOR
DETECTORS

THRUSTER GIMBAL
BEAM SHIELD UNIT

SOLAR CELL
MONITORS &
RADIATOR

C-82-5135
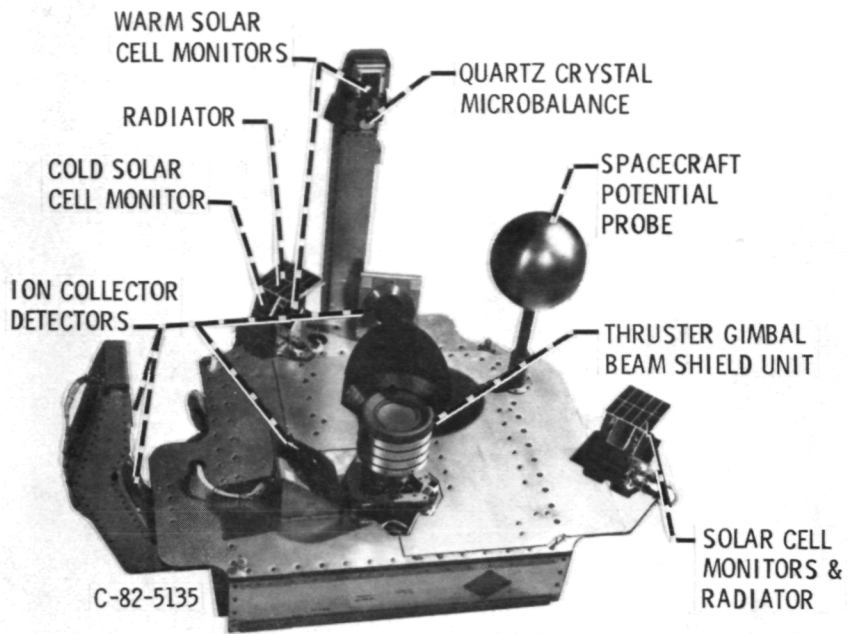
Figure 2. – Ion auxiliary propulsion system (IAPS) flight –Z module.

BEAM SHIELD

NEUTRALIZER

THRUSTER

GIMBAL

DIGITAL CONTROLLER
& INTERFACE UNIT
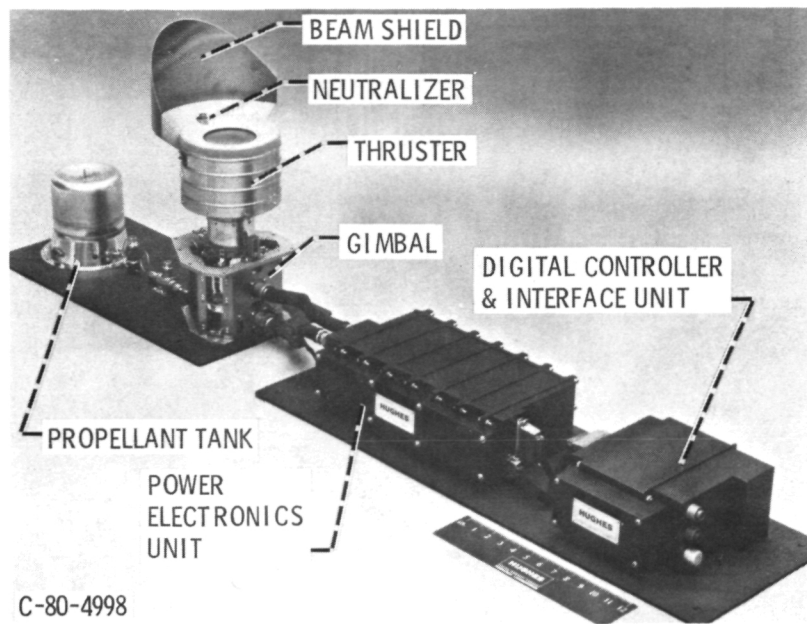
PROPELLANT TANK

POWER
ELECTRONICS
UNIT

C-80-4998

Figure 3. – IAPS thruster subsystem.
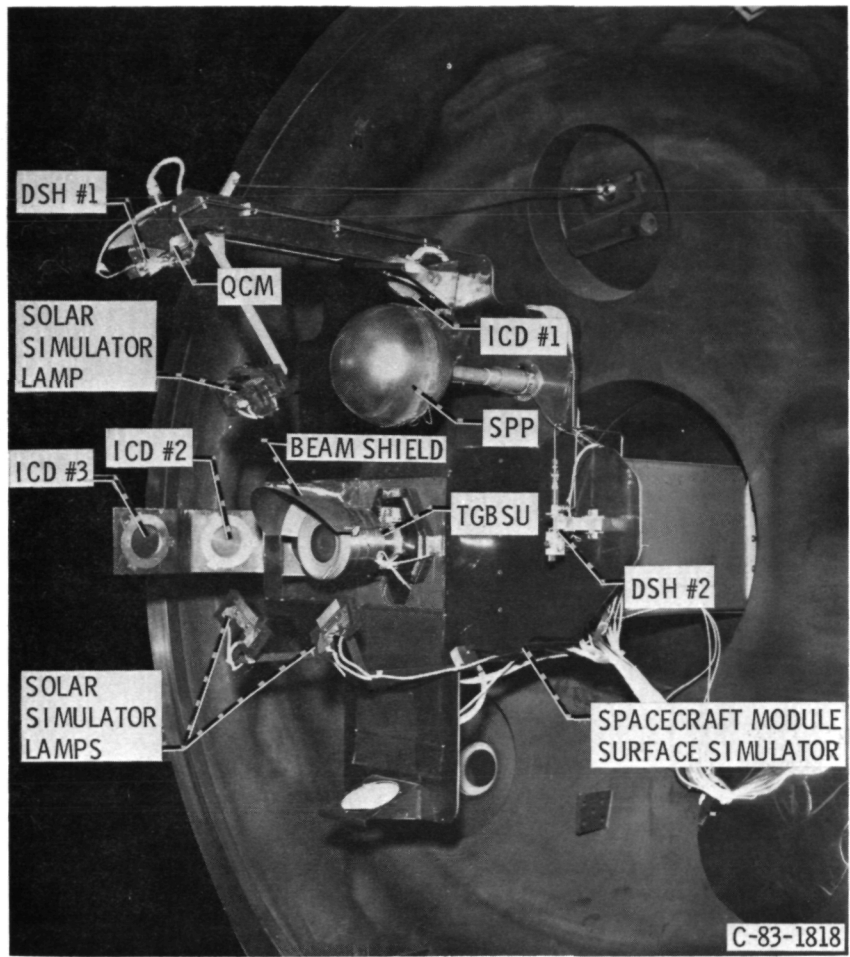
Figure 4. - Ground correlation test apparatus and configuration.

QCM
DSH #1   MOUNTED ON HIGH BOOM
ICD #1

HIGH BOOM

SPP

10°

BEAM
SHIELD

$58.0\ R$

49°

NEUTRALIZER

SHIELDED

$54.0\ R$

ICD #2,3

$60.0\ R$
BASIC
DIAGNOSTICS
RADIUS

A

SHORT
BOOM

A

ICD MOUNT
(not used)

THRUSTER

DSH #2

GIMBAL

GROUND PLANE
(wire mesh)

SPACECRAFT MODULE
SURFACE SIMULATOR

$\overline{\hspace{1cm}}$
10 cm

ICD MOUNT
(not used)

B
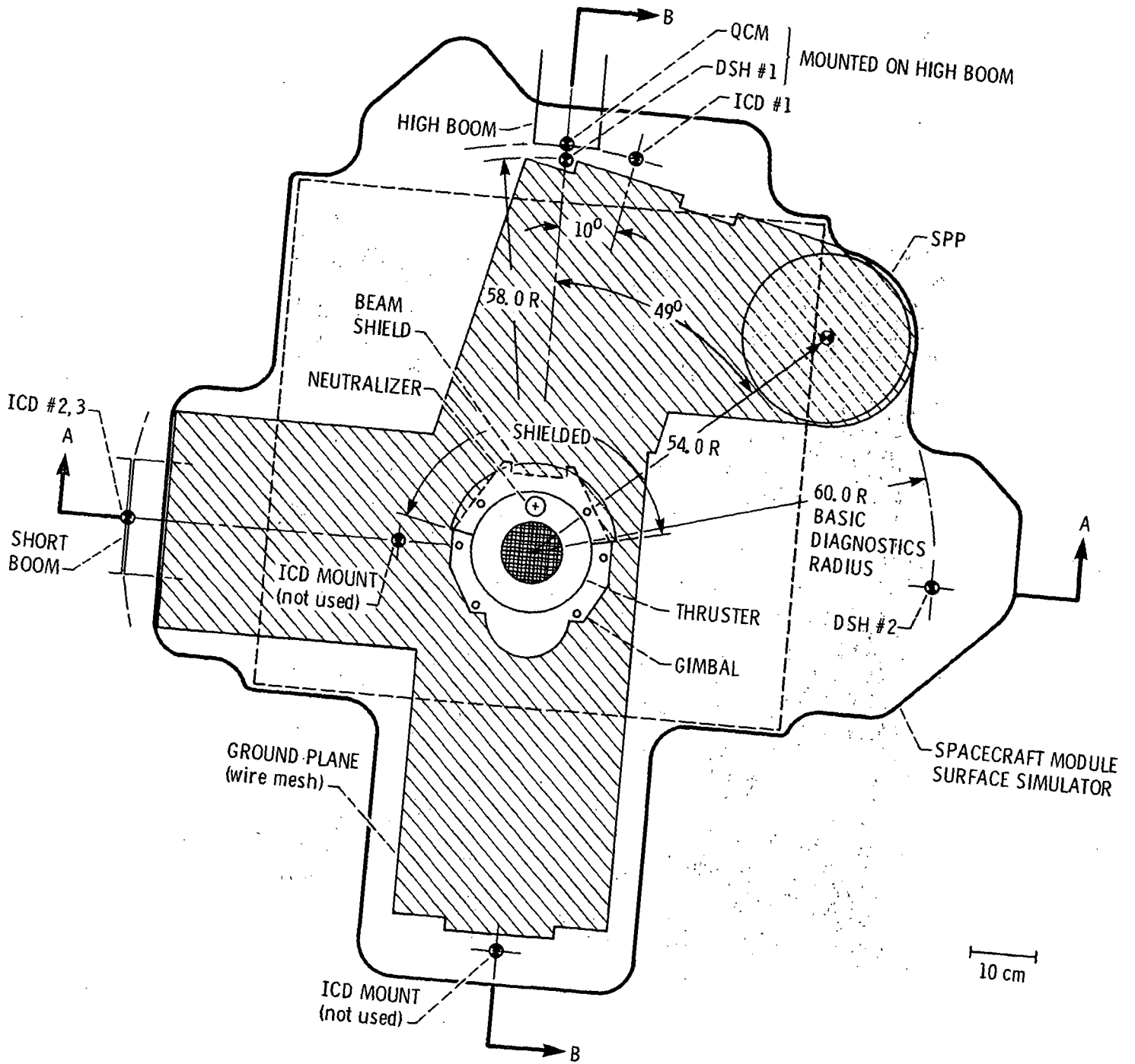
(a) Plan view. (Dimensions in cm.)

Fig. 5. - Ground correlation test configuration.

(b) A-A elevation view. (Dimensions in cm.)

Fig. 5. - Continued.
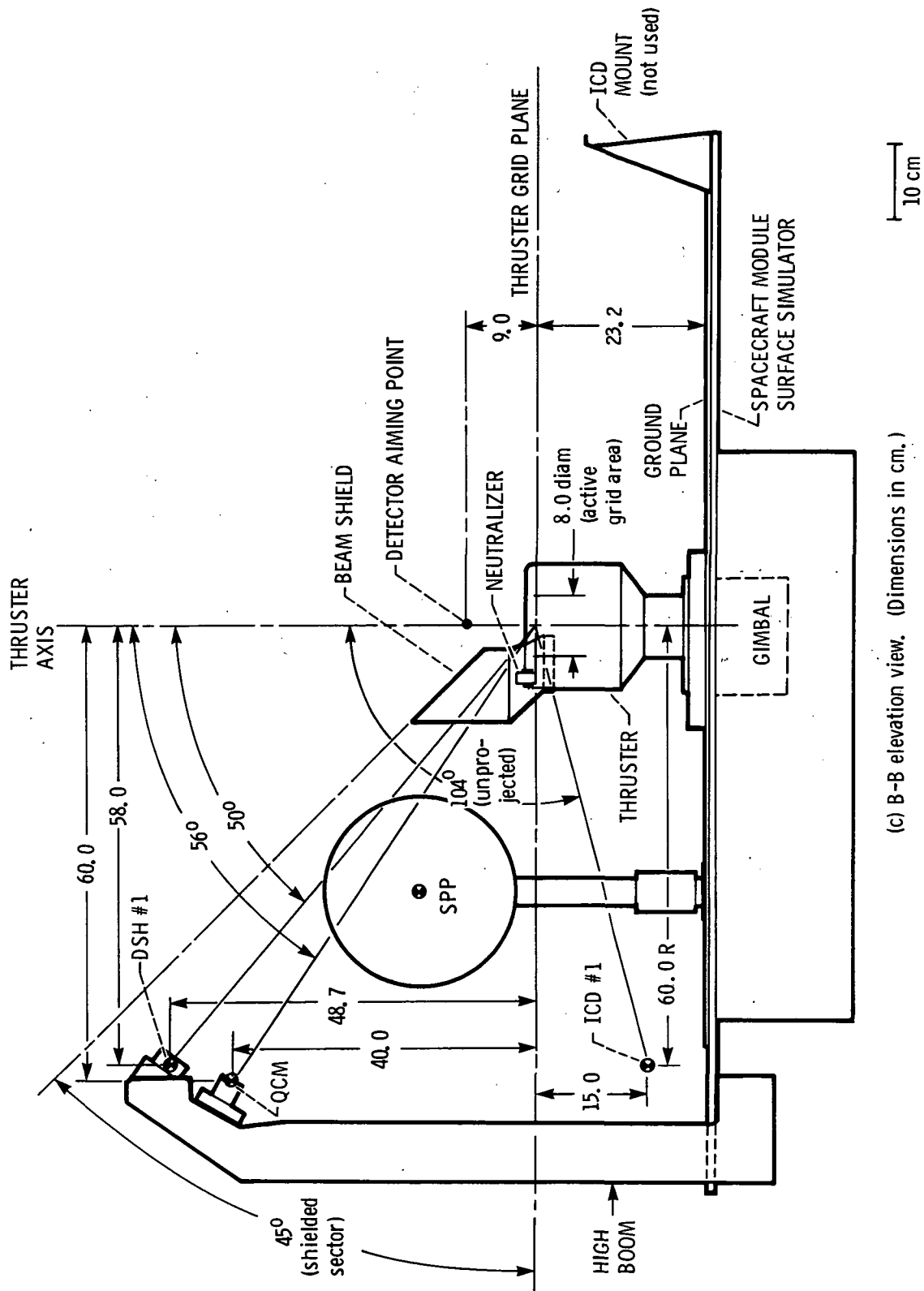
(c) B-B elevation view. (Dimensions in cm.)

Fig. 5. – Concluded.

10 cm

QUICK DISCONNECT
EVACUATION VALVE

MASK (outside
dimensions:
1. 85 x 1. 32 x 0. 057 cm)

AIR CYLINDER,
ACTUATING
SHUTTER

APERTURE
(0. 11 x 0. 61 cm)

SLIDE (exposed
area: 1. 19 x 0. 66 cm)

SHUTTER

THERMOCOUPLE

HEATER
(underside)

APERTURE
DIAPHRAGM
(0. 025 cm thick)

O-RING
SEALS

1. 31 cm

SHUTTER TOP AND BOTTOM
SURFACES TREATED WITH MoS$_2$

HEATER

MASK

SLIDE
(1. 91 x 1. 32 x 0. 16 cm)

1 cm

Fig. 6. - Deposition slide holder.

FRONT VIEW

GRID DETAIL (dimensions in mm, typical for all grids; open area, 72%)

13.97 diam

8.05 diam

7.49 diam

GROUNDING GRID

SHIELDING GRID

BIASING GRID

SUPPRESSOR GRID

COLLECTOR PLATE

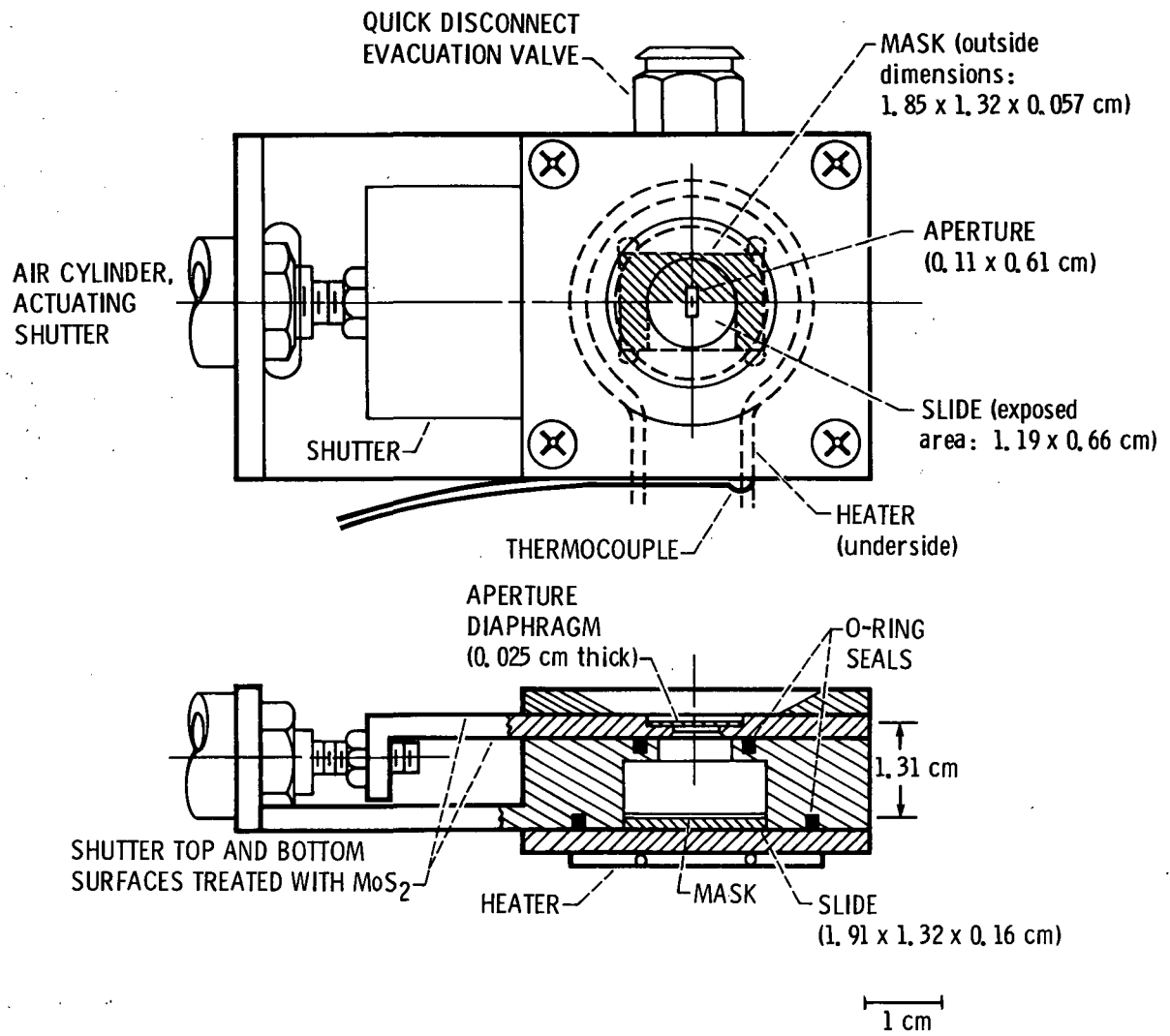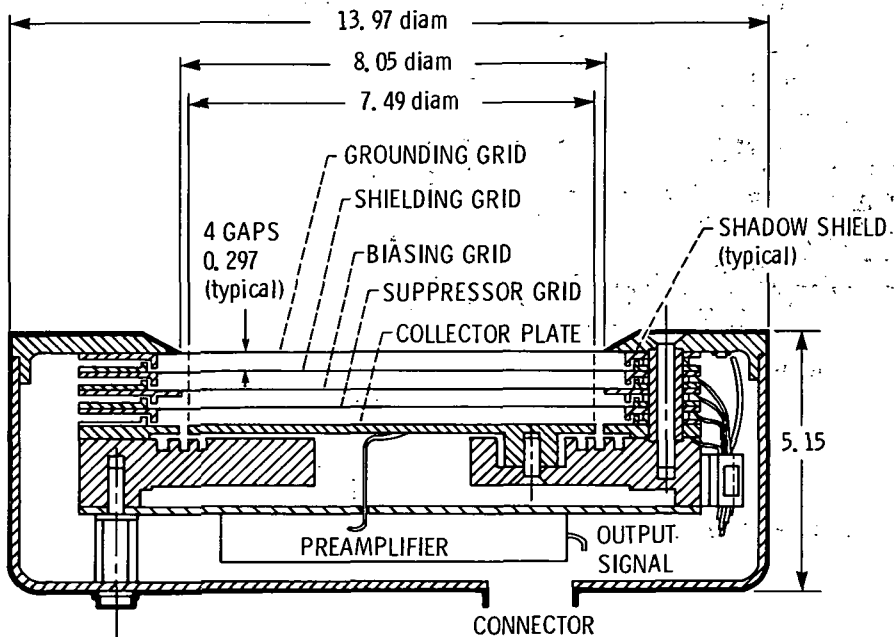SHADOW SHIELD (typical)

4 GAPS 0.297 (typical)

5.15

PREAMPLIFIER

OUTPUT SIGNAL

CONNECTOR
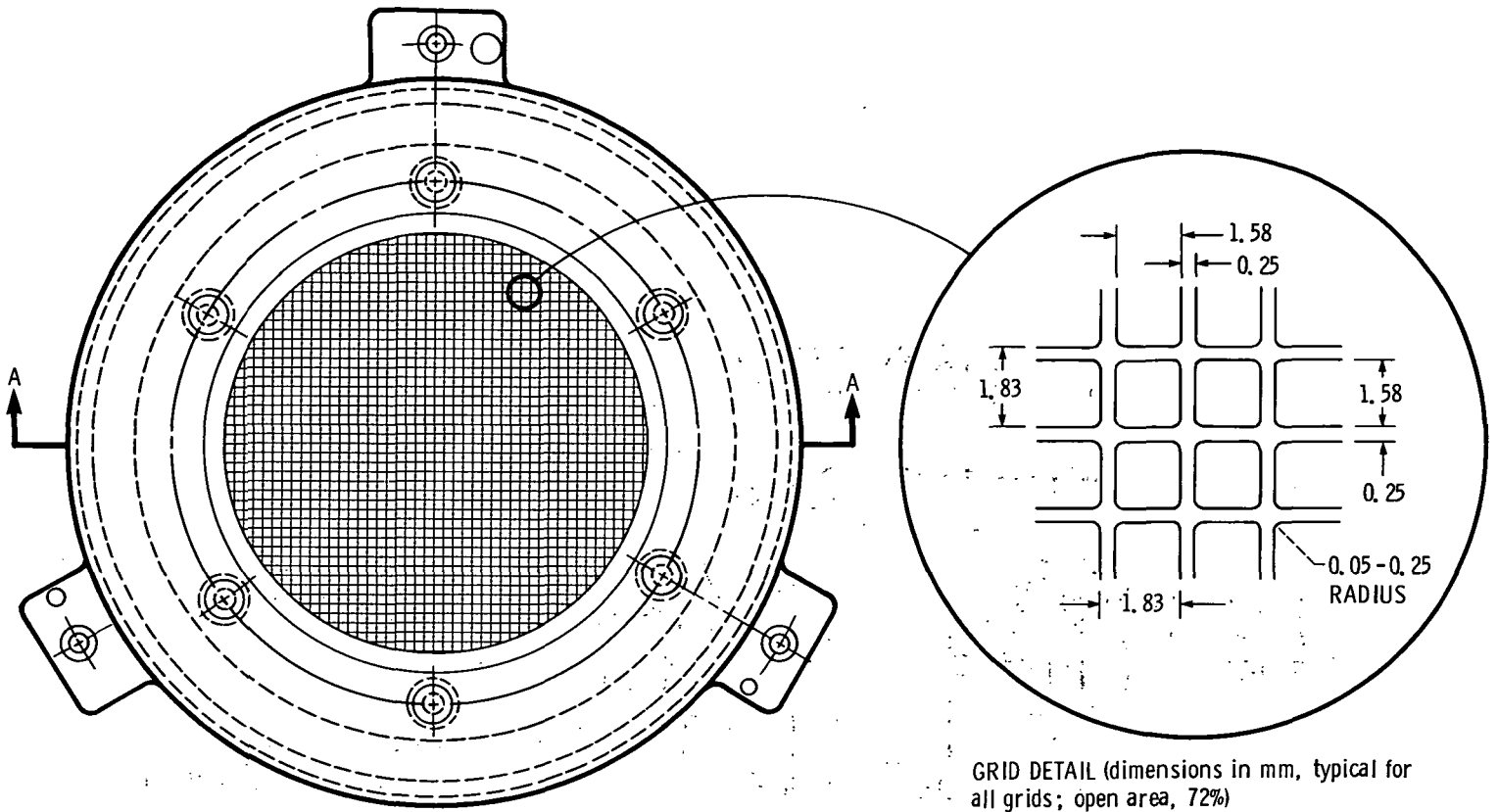
NORMAL POTENTIALS FROM CASE (SCC)
GROUNDING GRID: 0 V
SHIELDING GRID: -12 V
BIASING GRID: 0 TO +96 V
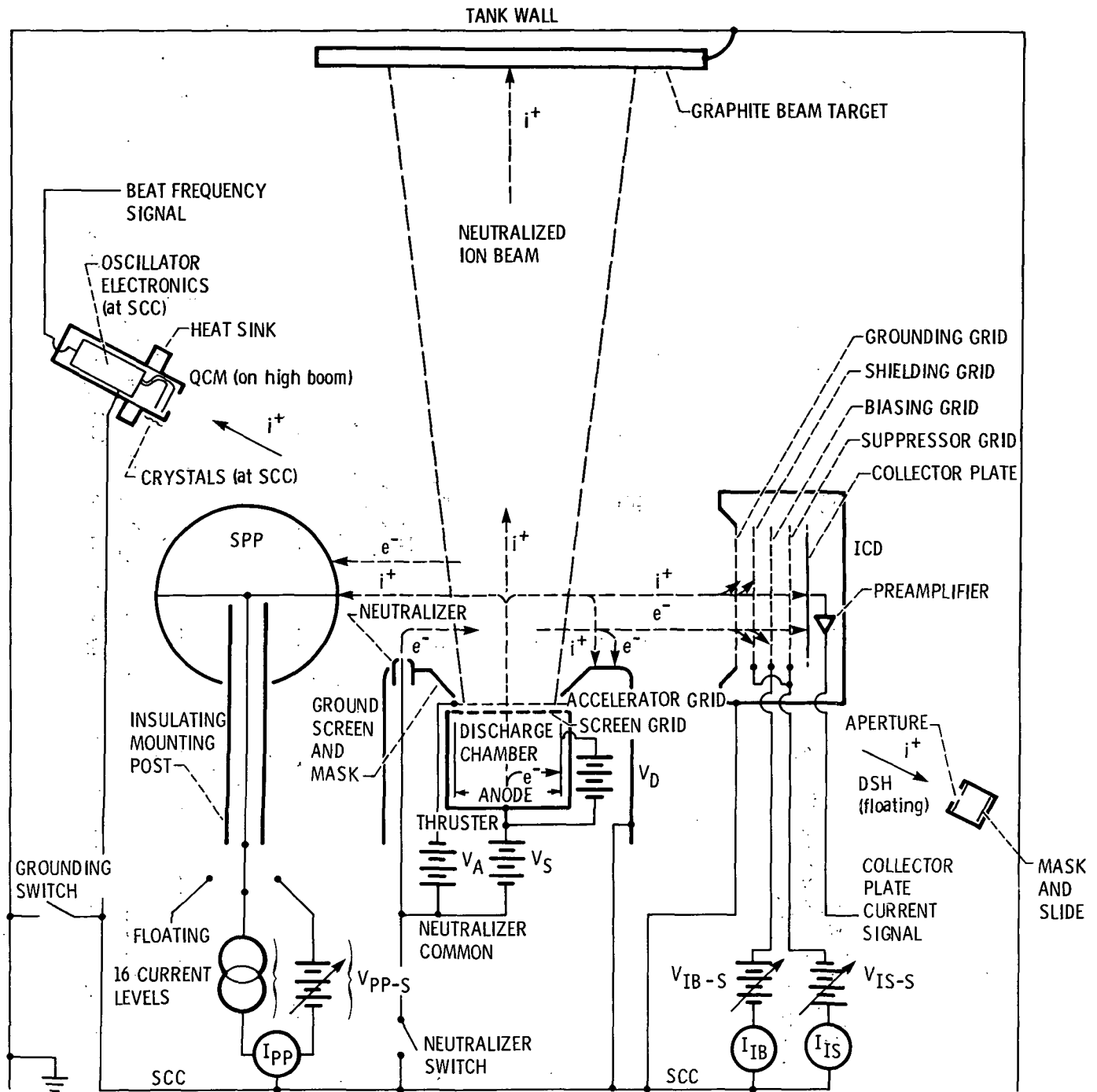SUPPRESSOR GRID: -12 V
COLLECTOR PLATE: 0 V

CROSS SECTION A-A

1 cm

Fig. 7. - Ion collector detector. (Dimensions in cm.)

TANK WALL

GRAPHITE BEAM TARGET

i^+

NEUTRALIZED
ION BEAM

BEAT FREQUENCY
SIGNAL

OSCILLATOR
ELECTRONICS
(at SCC)

HEAT SINK

QCM (on high boom)

i^+

CRYSTALS (at SCC)

GROUNDING GRID

SHIELDING GRID

BIASING GRID

SUPPRESSOR GRID

COLLECTOR PLATE

SPP

e^-

i^+

i^+

i^+

e^-

ICD

PREAMPLIFIER

NEUTRALIZER

e^-

i^+

e^-

INSULATING
MOUNTING
POST

GROUND
SCREEN
AND
MASK

DISCHARGE
CHAMBER

e^-

ANODE

ACCELERATOR GRID

SCREEN GRID

V_D

APERTURE

i^+

DSH
(floating)

GROUNDING
SWITCH

FLOATING

16 CURRENT
LEVELS

V_{PP-S}

THRUSTER

V_A V_S

NEUTRALIZER
COMMON

COLLECTOR
PLATE
CURRENT
SIGNAL

MASK
AND
SLIDE

V_{IB-S} V_{IS-S}

I_{PP}

NEUTRALIZER
SWITCH

SCC

I_{IB} I_{IS}

SCC

CONFIGURATION	NEUTRALIZER SWITCH	GROUNDING SWITCH
A	OPEN	OPEN
B	OPEN	CLOSED
C (not tested)	CLOSED	OPEN

SIGNIFICANT CURRENTS:
i^+ ION, e^- ELECTRON

Fig. 8. – Electrical schematic of thruster, power processor, and detectors for ground correlation testing.
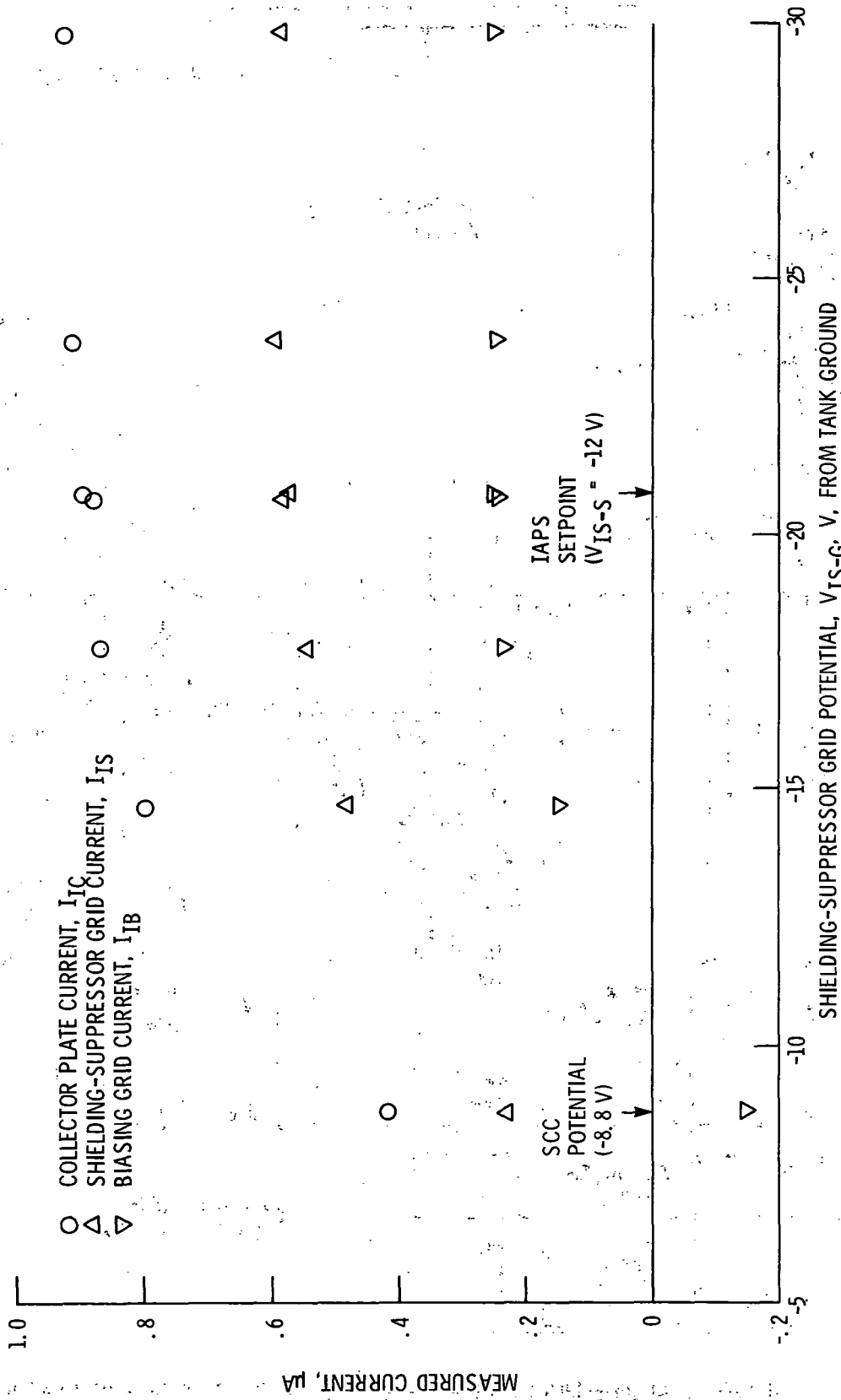
Fig. 9. – ICD #3 collector plate and grid currents versus shielding-suppressor grid potential. Configuration A; V_{IB-S} = +25 V (from SCC).
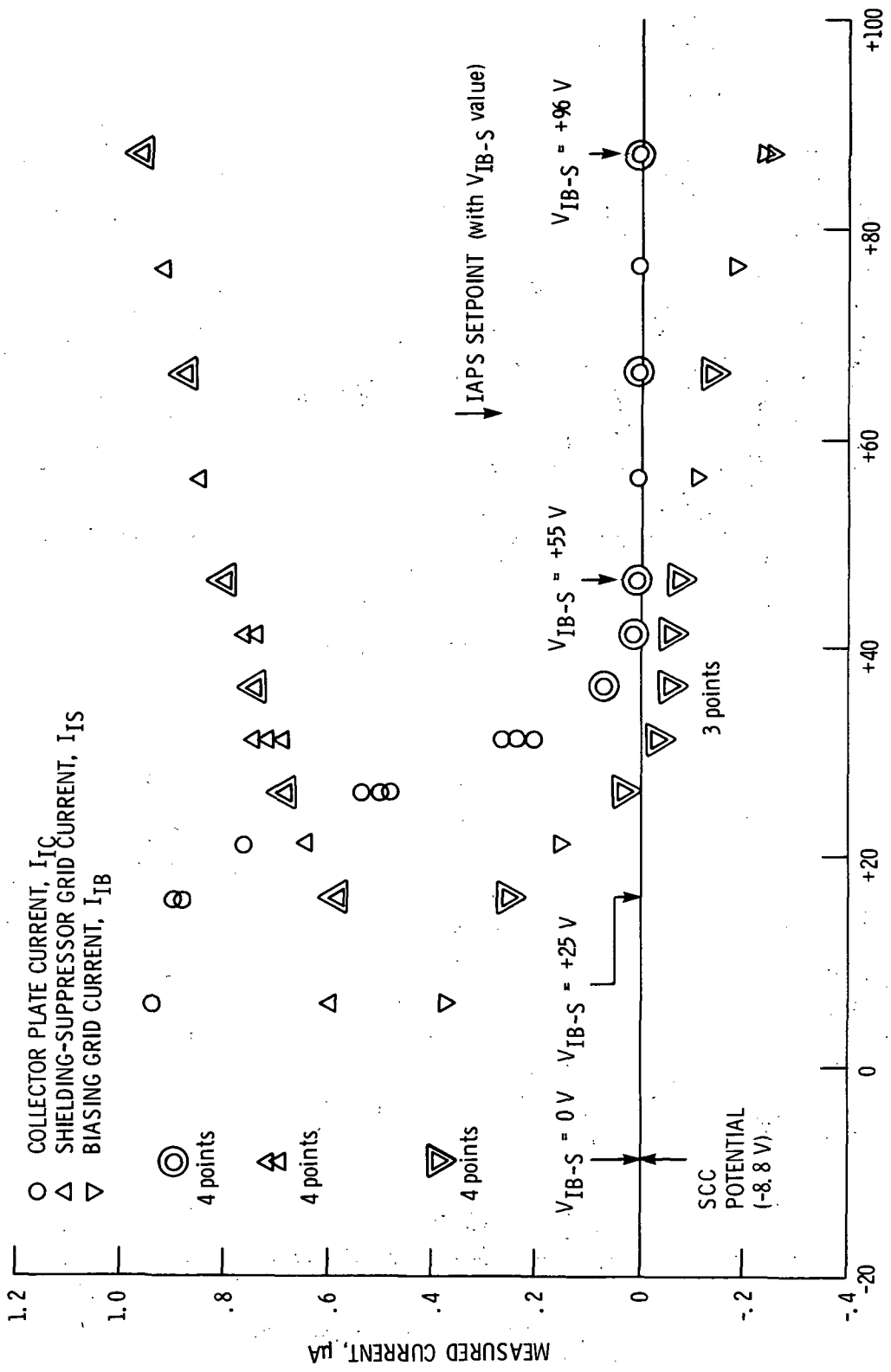
Fig. 10. - ICD #3 collector plate and grid currents versus biasing grid potential. Configuration A; $V_{IS-S} = -12$ V (from SCC).
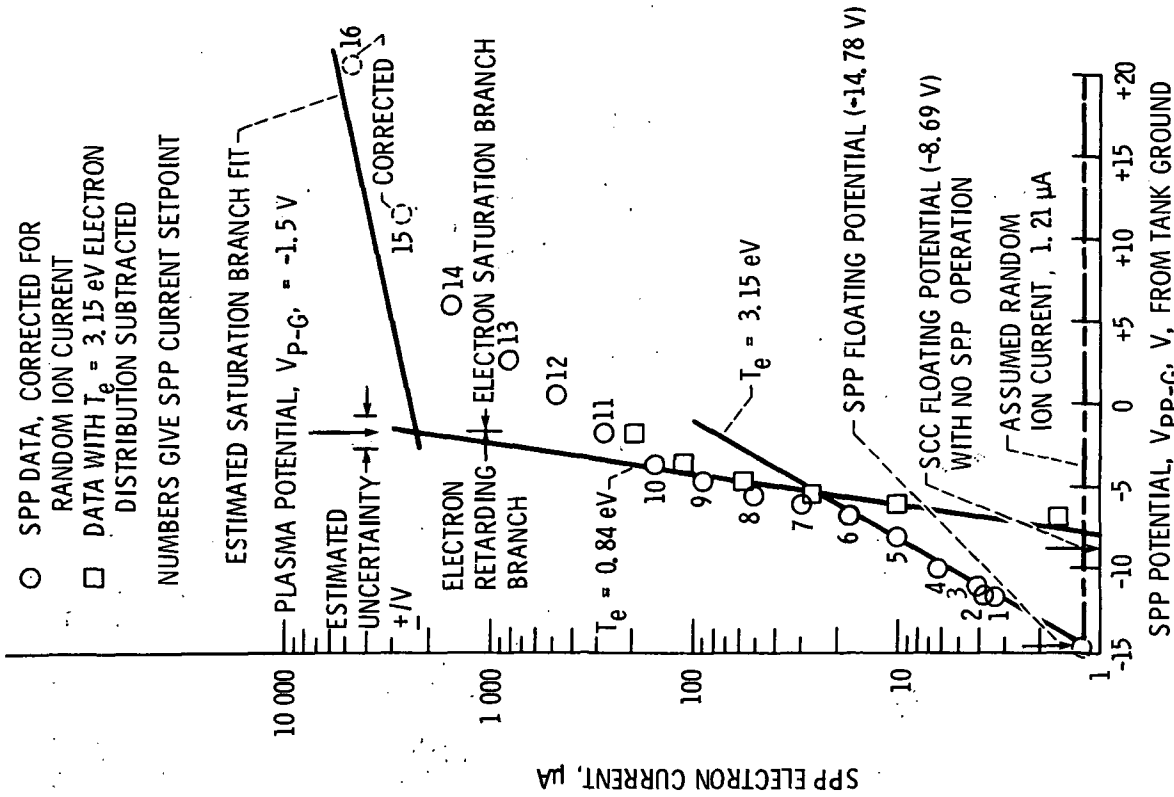
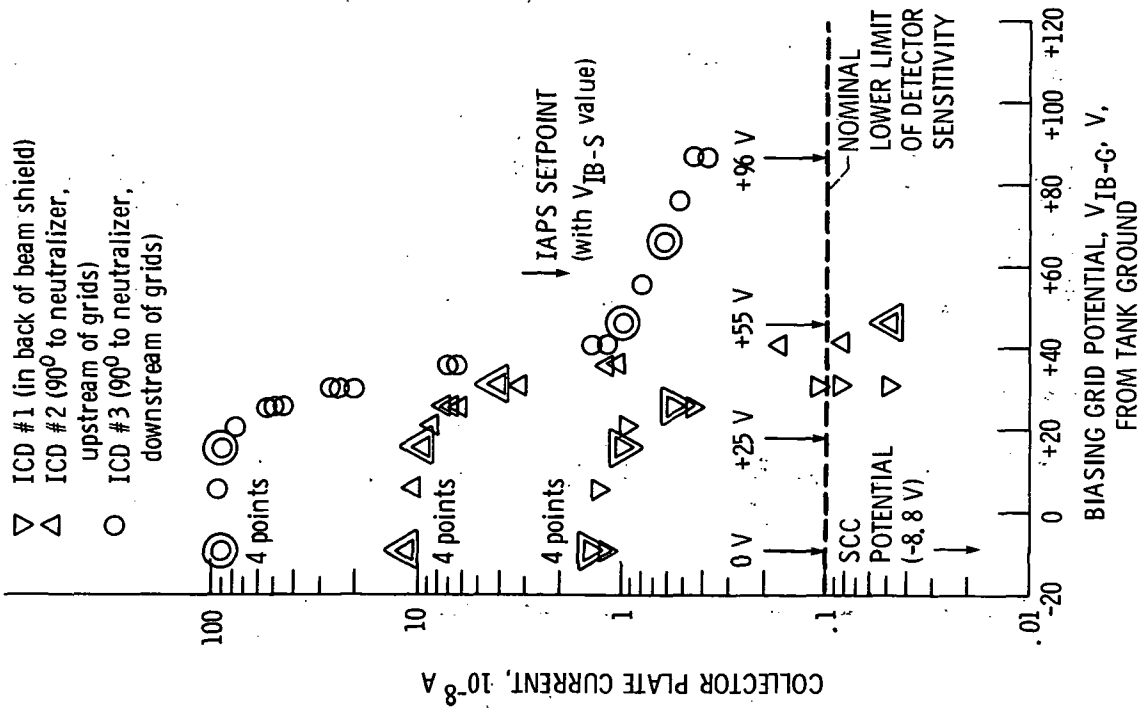Fig. 12 – Current-controlled electron collection on SPP. Configuration A.

O SPP DATA, CORRECTED FOR RANDOM ION CURRENT

□ DATA WITH T_e = 3.15 eV ELECTRON DISTRIBUTION SUBTRACTED

NUMBERS GIVE SPP CURRENT SETPOINT

ESTIMATED SATURATION BRANCH FIT

PLASMA POTENTIAL, V_{P-G} = -1.5 V

ESTIMATED UNCERTAINTY
+IV

ELECTRON RETARDING BRANCH

ELECTRON SATURATION BRANCH

CORRECTED

T_e = 0.84 eV

T_e = 3.15 eV

SPP FLOATING POTENTIAL (-14.78 V)

SCC FLOATING POTENTIAL (-8.69 V) WITH NO SPP OPERATION

ASSUMED RANDOM ION CURRENT, 1.21 µA

SPP ELECTRON CURRENT, µA

10 000   1 000   100   10   1

SPP POTENTIAL, V_{PP-G}, V, FROM TANK GROUND

-15   -10   -5   0   +5   +10   +15   +20

Fig. 11 – ICD collector plate currents versus biasing grid potential. Configuration A; V_{IS-S} = -12 V (from SCC).

▽ ICD #1 (in back of beam shield)

△ ICD #2 (90° to neutralizer, upstream of grids)

O ICD #3 (90° to neutralizer, downstream of grids)

4 points

IAPS SETPOINT (with V_{IB-S} value)

NOMINAL LOWER LIMIT OF DETECTOR SENSITIVITY

SCC POTENTIAL (-8.8 V)

0 V   +25 V   +55 V   +96 V

COLLECTOR PLATE CURRENT, 10^{-8} A

100   10   1   .1   .01

BIASING GRID POTENTIAL, V_{IB-G}, V, FROM TANK GROUND
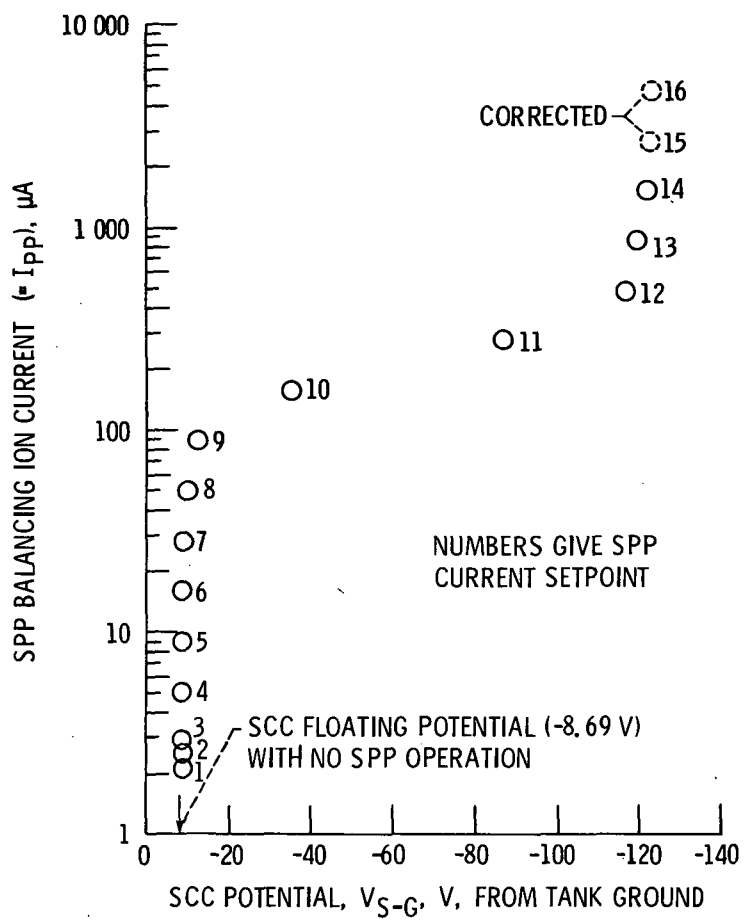
-20   0   +20   +40   +60   +80   +100   +120

Fig. 13. – Ion collection on SCC during current-controlled SPP operation. Configuration A.

1. Report No. NASA TM-83598	2. Government Accession No.	3. Recipient's Catalog No.
4. Title and Subtitle Ground Correlation Investigation of Thruster/Spacecraft Interactions to be Measured on the IAPS Flight Test		5. Report Date
		6. Performing Organization Code 542-05-12
7. Author(s) John L. Power		8. Performing Organization Report No. E-2007
		10. Work Unit No.
9. Performing Organization Name and Address National Aeronautics and Space Administration Lewis Research Center Cleveland, Ohio 44135		11. Contract or Grant No.
		13. Type of Report and Period Covered Technical Memorandum
12. Sponsoring Agency Name and Address National Aeronautics and Space Administration Washington, D.C. 20546		
		14. Sponsoring Agency Code

15. Supplementary Notes

Prepared for the Seventeenth International Electric Propulsion Conference cosponsored by the American Institute of Aeronautics and Astronautics, the Japan Society for Aeronautical and Space Sciences, and Deutsche Gesellschaft fur Luft- und Raumfahrt, Tokyo, Japan, May 28-31, 1984.

16. Abstract

Preliminary ground correlation testing has been conducted with an 8 cm mercury ion thruster and diagnostic instrumentation replicating to a large extent the IAPS flight test hardware, configuration, and electrical grounding/isolation. Thruster efflux deposition retained at 25° C was measured and characterized. Thruster ion efflux was characterized with retarding potential analyzers. Thruster-generated plasma currents, the spacecraft common (SCC) potential, and ambient plasma properties were evaluated with a spacecraft potential probe (SPP). All the measured thruster/spacecraft interactions or their IAPS measurements depend critically on the SCC potential, which can be controlled by a neutralizer ground switch and by the SPP operation.

17. Key Words (Suggested by Author(s)) Auxiliary propulsion; Mercury Ion Engines; Ion propulsion; Ground tests; Ion traps (Instrumentation); Electrostatic probes; Microbalances	18. Distribution Statement Unclassified - unlimited STAR Category 20	
19. Security Classif. (of this report) Unclassified	20. Security Classif. (of this page) Unclassified	21. No. of pages	22. Price*

SPECIAL FOURTH CLASS MAIL
BOOK

NASA